frontiers | Frontiers in Earth Science

TYPE Original Research
PUBLISHED 10 January 2023
DOI 10.3389/feart.2022.1032183

OPEN ACCESS

EDITED BY
Fei Xue,
Hohai University, China

REVIEWED BY
Qi Li,
China University of Geosciences, China
Zhenjun Sun,
Institute of Disaster Prevention, China
Xiaochao Shu,
China University of Mining and Technology, China

*CORRESPONDENCE
Gongwen Wang,
gwwang@cugb.edu.cn

SPECIALTY SECTION
This article was submitted to Economic Geology, a section of the journal Frontiers in Earth Science

RECEIVED 30 August 2022
ACCEPTED 03 November 2022
PUBLISHED 10 January 2023

CITATION
Xu Y, Wang G, Gao M, Yang W, Yang S, Yun H, Wu P, Guo N and Feng Y (2023), Genesis of the Shibaogou Mo–Pb–Zn deposit in the Luanchuan ore district, China: Constraints from geochronology, fluid inclusion, and H–O–S–Pb isotopes.
Front. Earth Sci. 10:1032183.
doi: 10.3389/feart.2022.1032183

Genesis of the Shibaogou Mo–Pb–Zn deposit in the Luanchuan ore district, China: Constraints from geochronology, fluid inclusion, and H–O–S–Pb isotopes

Yunchou Xu[1], Gongwen Wang[1,2,3]*, Meng Gao[1], Wangdong Yang[1], Shuren Yang[1], Hui Yun[4], Peijian Wu[5], Nana Guo[6] and Yantao Feng[7]

[1]School of Earth Science and Resources, China University of Geosciences, Beijing, China, [2]MNR Key Laboratory for Exploration Theory & Technology of Critical Mineral Resources, China University of Geosciences, Beijing, China, [3]Beijing Key Laboratory of Land and Resources Information Research and Development, Beijing, China, [4]Henan Institute of Geology, Zhengzhou, China, [5]Shandong Province Nuclear Industry Geological Group, Yantai, China, [6]Luoyang City Natural Resources Bureau, Luoyang, China, [7]Luanchuan Xinshu Weibo Mining Co., Ltd., Luoyang, China

The Shibaogou deposit is located in the Luanchuan ore district within the East Qinling orogenic belt (EQOB), central China, which is a newly discovered Mo–Pb–Zn skarn deposit. The skarn and Mo–Pb–Zn ore bodies are mostly hosted in the contact zones between the Shibaogou porphyritic granite and carbonaceous sedimentary rocks from the Luanchuan and Guandaokou sets. A study combined of geochronology, fluid inclusion (FI), and stable isotopes was performed to constrain the mineralization age, source of ore materials, and the origin and evolution of the ore-forming fluids and their relationship with the subduction of the Paleo-Pacific Plate. The mineralization process includes skarn and quartz–sulfide episodes, which has four stages: skarn (I), quartz–molybdenite (II), quartz–galena–sphalerite (III), and quartz–calcite (IV). Molybdenite Re-Os dating suggests that the deposit was formed in the Late Jurassic (147.4 ± 7.2 Ma). Reportedly, there are five primary types of fluid inclusions: L-type, V-type, H-type, S-type, and C-type. In the skarn stage, coexisting H-type (35.58 wt%–46.05 wt% NaCl equiv.) and low-salinity V-type (0.35 wt%–5.7 wt% NaCl equiv.) fluid inclusions show similar homogenization temperatures, which suggests that fluid boiling occurred at 513–550°C and 580–650 bar (2.19–2.45 km). In the quartz–molybdenite stage, the homogenization temperatures of L-type, V-type, minor H-type, and S-type fluid inclusions indicate continued fluid boiling at 324–387°C and 180–250 bar (0.49–0.94 km). In the quartz–galena–sphalerite stage, a fewer number of coexisting V-type and L-type fluid inclusions in quartz shows different salinities with similar homogenization temperatures, indicating that they are trapped at 303–347°C and <150 bar in the boiling process (<0.56 km hydrostatic depth). The minor primary L-type fluid inclusions that have lower salinities of 0.88 wt%–11.34 wt% NaCl equiv were observed in quartz and calcite in the

quartz–calcite stage; in addition, their homogenization temperatures are 103–247°C (typical post-ore conditions). This study found that the ore-forming fluids at the Shibaogou deposit were dominantly magmatic water at the early stage, with input of atmospheric water during fluid evolution, with $\delta^{18}O_{fluid}$ values from –1.168‰ to 8.997‰ and $\delta^{18}D_{fluid}$ values from –106.5‰ to –79.9‰, based on the O and H isotope data from garnet, quartz, and calcite. Furthermore, the S isotopic compositions were measured ranging from 0.8‰ to 14.7‰, and it demonstrated that the ore-forming fluid was mainly derived from magmatic sources. The relatively homogeneous Pb isotopic compositions are similar to those of Shibaogou granite porphyry, which demonstrated that the ore-forming materials were mainly derived from magmatic sources. Molybdenite was precipitated as a result of fluid–rock interactions and fluid boiling, and the galena and sphalerite were precipitated as a result of the decreasing temperature. The subduction of the Paleo-Pacific plate has a critical impact on the complex evolution of ore formation in the Shibaogou skarn deposit in EQOB.

KEYWORDS

molybdenite Re-Os age, fluid inclusion, H–O–S isotopes, Shibaogou Mo–Pb–Zn, Luanchuan ore district

1 Introduction

During the Mesozoic, the lithosphere in and around northeast China was thinned and extended on a large scale because of the subduction of the Paleo-Pacific plate into the Eurasian plate, resulting in not only strong magmatism but also extensive metallogenic events (Hua and Mao, 1999; Mao et al., 2005,2013; Ouyang et al., 2013; Xue F et al., 2021). The East Qinling molybdenum (Mo) belt (EQMB) hosting the largest Mo ore district on the earth (Mao et al., 2011; Zeng et al., 2013) provides excellent areas to study the genetic relationship between the Paleo-Pacific Plate subduction and the mineralization in eastern China (Mao et al., 2011; Zeng et al., 2013). Up to date, most studies are about the deposit type, mineralization ages, evolution of ore-forming fluids, and their geodynamic setting (Li et al., 2007, 2013; Mao et al., 2011; Zeng et al., 2013).

In recent mineral exploration events in the EQMB, some typical skarn-type Mo deposits have been found whose genesis is still debated. Skarn-type deposits are formed from the complex metasomatic processes between carbonate-rich rocks and hydrothermal fluids. They are essential sources for W, Cu, Fe, Zn, Pb, Ag, and Au but seldom for Mo (Newberry and Swanson, 1986; Hedenquist and Lowenstern, 1994; Meinert et al., 2005; Marcoux et al., 2019; Tang et al., 2021; Tang et al., 2022). Therefore, some controversies are remaining on the metallic and fluid sources of skarn-type Mo deposits, including igneous and sedimentary rocks (Yokoro et al., 2013), and other wall rocks (Gemmell et al., 1992).

The Shibaogou deposit is a typical skarn-type Mo (Pb–Zn) in the Luanchuan ore district (LOD) within the EQOB. The Shibaogou deposit contains 87,000 t Mo (avg. 0.11%),79,614 t Pb (avg. 4.2%), and 73,141 t Zn (avg. 3.86%). Xue et al. (2018) reported the petrogenesis and geochronology of the ore-related Shibaogou granitic intrusions; however, the source and evolution of the ore-forming fluids of the Shibaogou skarn-type Mo (Pb–Zn) deposit remain poorly elucidated. The present study showed the new data on molybdenite Re-Os ages, as well as fluid inclusions and H–O–S–Pb isotopes. We aim to determine the mineralization age and source of ore materials and to understand the characteristics of the ore-forming fluids and their evolution, eventually revealing the metallogenic genesis and providing evidence to explore the impact of the subduction of the Paleo-Pacific Plate on the mineralization within the East Qinling orogenic belt.

2 Local geology

The Luanchuan ore concentration area has played an important economic role in the production of Mo–W–Pb–Zn–Ag minerals (Figure 1). In the East Qinling area, Mo > 1.5 Mt, ~ 0.5 Mt WO_3, 7 Mt Pb and Zn, and 8000 t Ag ore belt were discovered (Mao et al., 2011; Wang et al., 2019). Shibaogou is located on the southern edge of the North China Craton. The Luanchuan fault zone, North China Craton to the north, and North Qinling fold system to the south define the tectonic units. The main strata in this area are the Mesoproterozoic Guandaokou Group, Kuanping Group, Neoproterozoic Luanchuan Group, and Paleozoic Taowan Group. The Mesoproterozoic sedimentary rocks are composed of sandstone, dolomite, greenschist, and a small amount of quartzite, which are partially interbedded with marble. The

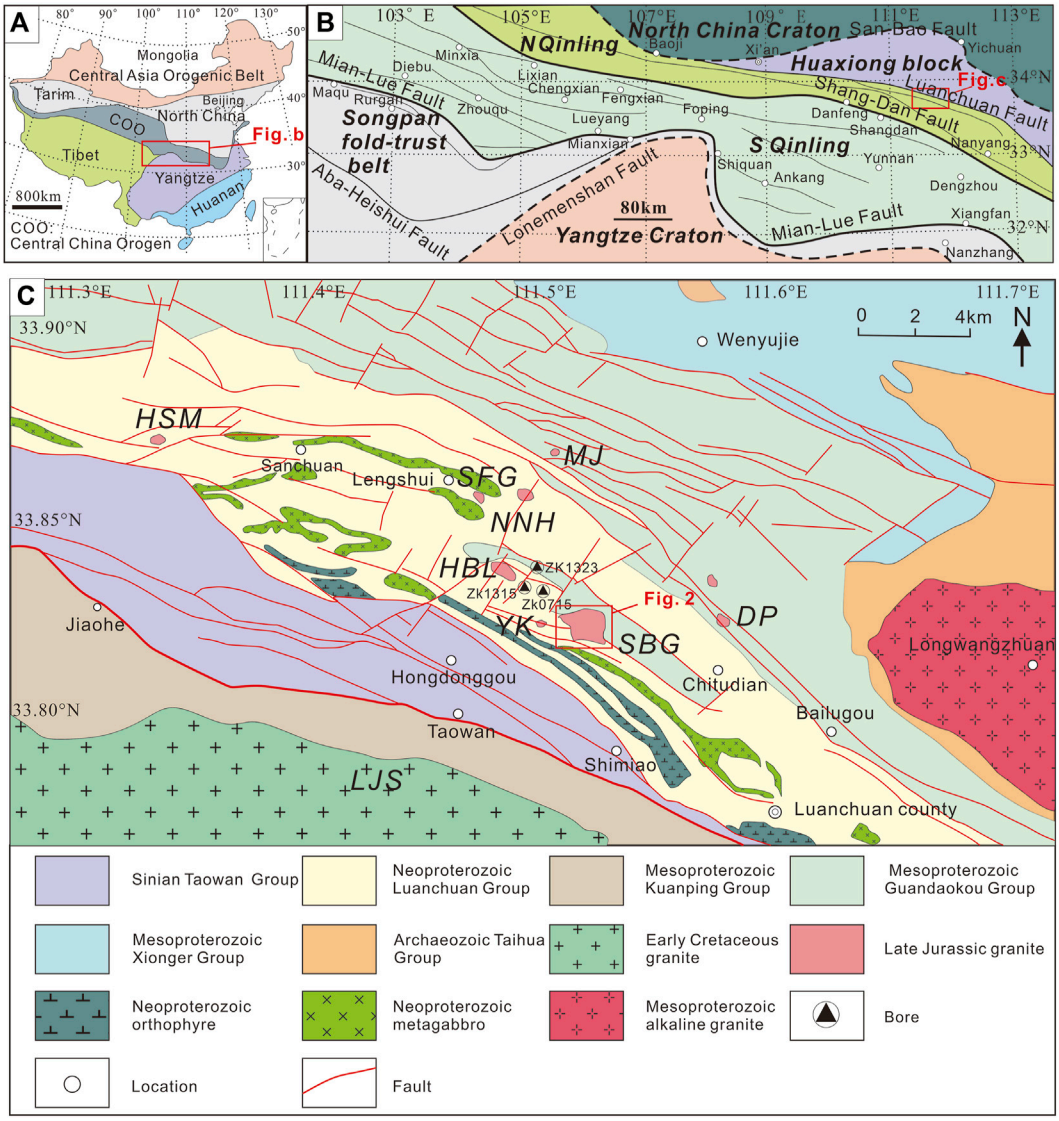

FIGURE 1
(A) Tectonic map of China showing the location of Central China belt and North China Craton; **(B)** tectonic subdivision of the Qinling Orogen showing the location of Luanchuan ore district; and **(C)** geological map of Luanchuan ore district displaying the geology and the distribution of granites, modified after Duan et al. (2010), Mao et al. (2011) and Yang et al. (2016). YK, Yuku; SBG, Shibaogou; HBL, Huangbeiling; NNH, Nannihu; SFG, Shangfanggou; MJ, Majuan; DP, Daping; HSM, Huoshenmiao; and LJS, Laojunshan.

Luanchuan Group is composed of dolomite and schist, and the Taowan Group is composed of limestone, schist, and conglomerate. The sedimentary unit of the Luanchuan mining area (Figure 1) is intruded by extensive Late Jurassic to Early Cretaceous porphyritic granites and a small amount of contemporaneous quartz diorites. The main structures of the Luanchuan mining area are the WNW-ESE-trending Luanchuan and Miaozi faults, and the NE-SW-trending Huangbeiling–Nannihui–Maquan and Shibaogou–Zhuangke faults. Mesozoic LOD magmatic activity was particularly intense and widespread, forming a broad range of generations of granites associated with molybdenum, tungsten, gold, silver, copper, galena, and sphalerite mineralization. Granite porphyry is the most common and important parent rock for molybdenum mineralization, with phenocrysts of quartz (20%–35%), potassium feldspar (40%–55%), plagioclase (10%), and, occasionally, black Mica. According to the zircon U–Pb dating results, the porphyritic granites were in place in a relatively short period of 158–141 Ma (Mao et al., 2005; Li et al., 2015; Xue et al., 2018).

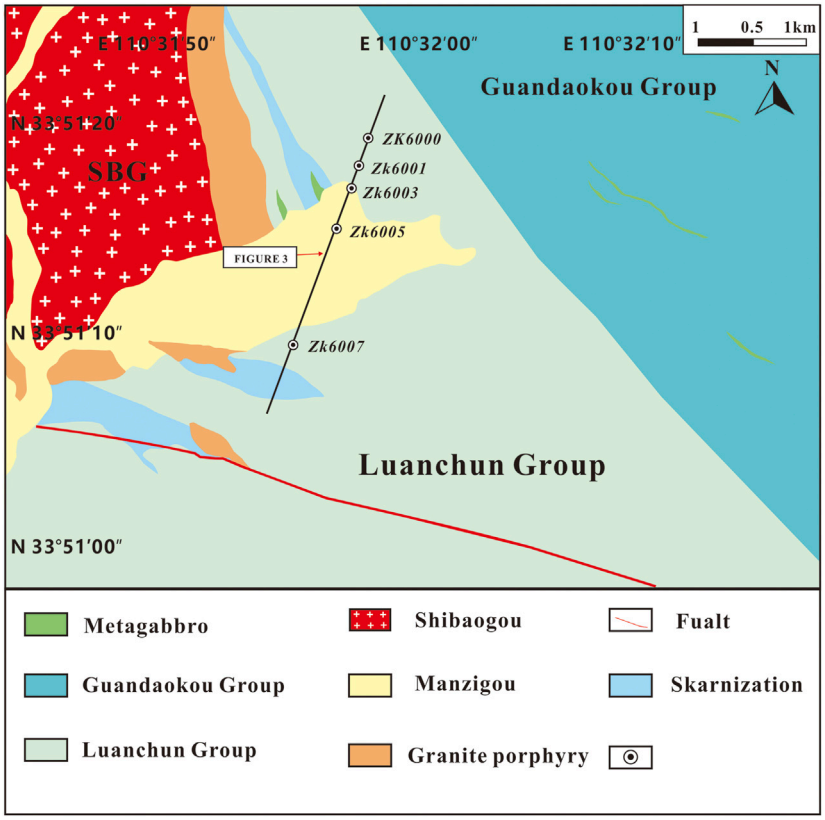

FIGURE 2
Geology of the Luanchuan ore district showing the Shibaogou Mo–Pb–Zn deposit (after Xue L. W et al., 2021).

3 Deposit geology

3.1 Geology

The Luanchuan Group has abundant mineral resources, including galena–sphalerite ore, iron ore, vanadium ore, stone coal, and other types of ore. The Xiaohonggounao–Xiaolaohugoukou Fault, Maquan–Daping Fault, and Huangbeiling–Shibaogou Fault have all developed, with the latter two faults compounded near Guodian. In total, two dense belts of the north (north) east-trending faults are the Huangbeiling–Nanihu–Maquan belt and Shibaogou–Qinghetang fault dense belt. The sedimentary rocks related to the Shibaogou deposit comprise the Guandaokou and Luanchuan groups (Figures 2, 3), which consist mainly of marble, metasandstone, schist, and quartzite. In the Shibaogou Mo–Pb–Zn deposit, the Guandaokou group is mainly the Baishugou Formation and the Luanchuan group is dominantly Sanchuan, Nannihu, and Meiyaogou formations. The Meiyaogou Formation is in fault contact with the Baishugou Formation and has a conformable contact with the Nannihu Formation. The Shibaogou granite porphyry intrudes into the Guandaokou group and Luanchuan group, and intrudes into the Guandaokou group more. The mineralization is also mostly in the place where the Shibaogou granite porphyry contacts with the Guandaokou group. A total of five economic Mo ore bodies (No. 1–5) have been found at the Shibaogou deposit, in which the number 1 ore body is of greatest worth. The Mo-1 ore body is the largest molybdenum ore body in the mining area. It is located between the Heng 72 exploration line and the 58 exploration line. The occurrence elevation is 534–1245 m, the minimum is 339 m, the true thickness of a single project is 16.19–59.57 m, the average true thickness is 38.89 m, and the thickness variation coefficient is 45.12%. A total of nine economic Pb–Zn ore bodies (No. 1–9) have been explored at the Shibaogou deposit, and the No. 1 ore body was found the greatest worth. It is 1400 m long and 0.41–1.85 m wide. The ore body has obvious rock-control characteristics as a whole, and it often occurs in the lower side of the strata of the upper Meiyaogou Formation and in siliceous stripe (zone) of dolomite marble within 20–30 m of the lower part of the carbonaceous slate, and the thickness is of a stable type alteration and mineralization.

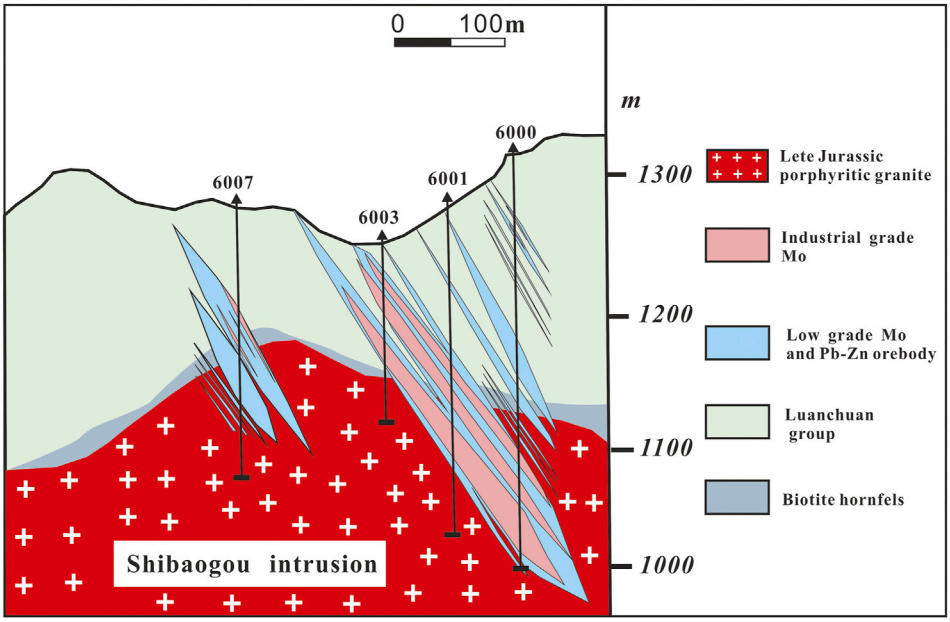

FIGURE 3
Geological map of the Shibaogou Mo–Pb–Zn deposit geologic cross section showing the spatial relationship among strata, intrusion, alteration, and ore bodies.

3.2 Alteration and mineralization

3.2.1 Skarn stage (stage I)

3.2.1.1 Prograde skarn stage

The Shibaogou skarn Mo deposit has a typical skarn prograde alteration assemblage. Based on field observation, the rock types vary from inner Shibaogou granite porphyry to outer garnet–pyroxene skarn, pyroxene–garnet skarn, and garnet–wollastonite skarn termed as a prograde alteration. The prograde skarn occurs as an initial alteration assemblage. This stage is dominated by anhydrous fine-to-coarse-grained (0.06–4 mm) and euhedral-to-subhedral crystal garnet minerals (Figures 4A,E,G), which were developed widely in the Shibaogou deposit. In addition, pyroxene minerals exhibit colors of light grayish to dark green and sizes of 0.06–2.5 mm (Figure 4F). Wollastonite minerals are sometimes associated with garnet minerals occurring near the marbles as subhedral radiating clusters (Figures 4G, 5A–C).

3.2.1.2 Retrograde skarn stage

Compared to other skarn deposits, the Shibaogou Mo deposit is characterized by weakly developed retrograde skarns, which are dominated by epidote minerals forming together with interstitial quartz (Figures 4H, 5E), or as replacements of garnet minerals. They are euhedral to subhedral with variable sizes from 0.03 up to 1 mm occurring as veins cutting the pyroxene–garnet skarn.

3.2.2 Quartz–molybdenite stage (stage II)

Quartz–molybdenite veins that have a length of 3–50 cm are the main economic product at the dominant mineralization stage in the shibaogou deposit. A large number of platy molybdenite minerals occur at the edges of quartz veins in contact with skarn minerals or in disseminated form in garnets (Figures 4B,F,J, 5D–F), while some fine-grained crystals assembled in flakes along the veinlet walls. In addition, a few clumps of quartz–molybdenite veins developed in banded garnet and pyroxene skarns. These veins crosscut pyroxene and altered garnet minerals, implying that they formed after garnet and pyroxene in the skarn stage (Figure 4K).

3.2.3 Quartz–galena–sphalerite stage (stage III)

The quartz–galena–sphalerite stage is another important metallogenic stage in the Shibaogou deposit generating various sulfides including pyrite, sphalerite, galena, and chalcopyrite. Among these sulfides, galena is the major ore mineral, which is commonly leaden-colored but varies from fine to coarse grained occurring with sphalerite as intergranular aggregates (Figures 5G–I). They also occur together with quartz grains, cutting across that quartz–molybdenite vein (Figures 4C,D).

3.2.4 Carbonate stage (stage IV)

During the post-mineralization stage, some low-temperature alteration minerals formed consisting of dominant calcites, which occur as veinlets crosscutting skarn and sulfides (Figure 4M).

FIGURE 4
(A) Calcite–quartz vein cross-cutting a quartz–molybdenum–vein molybdenum; **(B)** molybdenum mineralization in skarn; **(C)** galena mineralization in the quartz–galena–sphalerite stage; **(D)** galena mineralization coexisting with pyrite in the quartz–galena–sphalerite stage; **(E)** molybdenum mineralization in garnet skarn; **(F)** molybdenum–quartz vein cross-cutting pyroxene skarn; **(G)** wollastonite skarn (Wo>Grt>Pyx); **(H)** chlorite alteration overprinting skarn; **(I)** dikes intrude into ore bodies; **(J)** galena–sphalerite–quartz vein cross-cutting molybdenum–quartz vein; **(K)** quartz–sulfide vein cross-cutting molybdenum–quartz vein; **(L)** galena mineralization coexisting with sphalerite in the quartz–galena–sphalerite stage; and **(M)** calcite–quartz vein cross-cutting molybdenum–quartz vein and garnet skarn (Grt>Pyx). Chl = chlorite; Gn = galena; Grt = garnet; Mo = molybdenite; Py = pyrite; Pyx = pyroxene; Q = quartz; Sph = sphalerite; and Wo = wollastonite.

4 Sampling and analytical methods

4.1 Microthermometry and laser Raman spectroscopy

Quartz and calcite inclusions that are fluid-filled were studied throughout multiple hydrothermal phases. In Beijing, in Chinese College of Technology and Academic Research, the Linkam THMSG600 high-temperature chiller and the Zeiss microscope was employed to implement experimental fluid inclusions micromeasurement. The 195 to + 600°C fluid inclusions was frozen at 150°C degrees and gradually heated to complete uniformity. Near the phase transition, the heating/freezing rate is 15°C/min, and the low temperature is 1–0.1°C/min. The ultimate ice melting point was employed to establish the concentration of salt of the inclusion complex that incorporated water (NaCl H_2O). Accessing the approach developed by Sterner et al. (1988), the salinity of insertion coordination compounds limestone salts (high salt) was approximated (Collins, 1979). The salt concentration of aqueous (NaCl H_2O) or CO_2 actually contains elements served as a

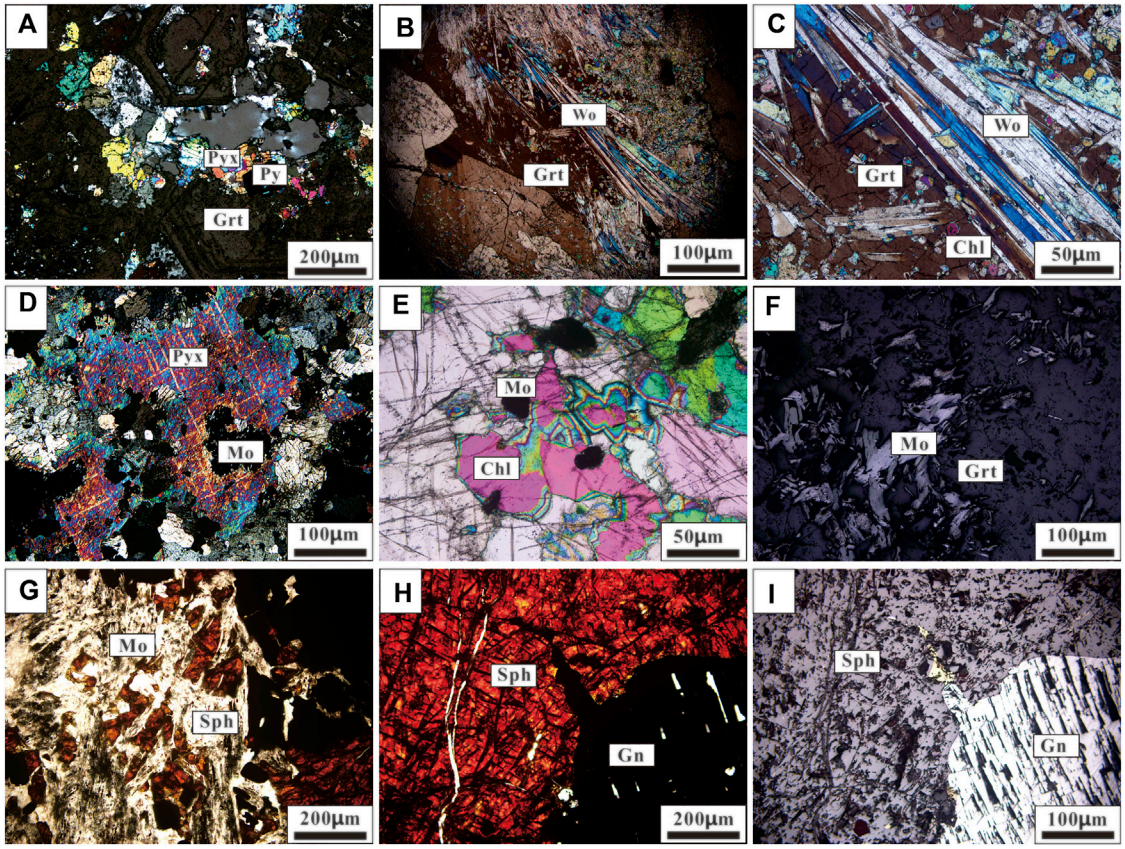

FIGURE 5
(A) Garnet skarn (Grt>Pyx); **(B)** wollastonite skarn (Wo>Grt>Pyx); **(C)** wollastonite skarn (Wo>Grt>Pyx). Chlorite alteration overprinting garnet skarn; **(D)** pyroxene with clear orthorhombic cleavage coexisting with molybdenum; **(E)** chlorite alteration; **(F)** molybdenum mineralization in the quartz–sulfide stage; **(G)** molybdenum coexisting with galena and sphalerite; and **(H–I)** galena coexisting with sphalerite in the quartz–galena–sphalerite stage. Chl = chlorite; Gn = galena; Grt = garnet; Mo = molybdenite; Py = pyrite; Pyx = pyroxene; Q = quartz; Sph = sphalerite; and Wo = wollastonite.

premise for estimation methods (daughter ore that is invisible or translucent).

For an optical analysis, upwards of 50 quintuple grinding discs have been manufactured, and 18 representative participants were taken for micro-temperature detection and Raman spectroscopic–independent inquiry. The Chinese Training Institute of Geographical Studies' Hydraulic Addition Center in Beijing, China, used RM-2000 optical Raman spectrometer to characterize the structure of water exclusions. The Ar^{+} laser really does have a spectral resolution of 1 cm^{-1}, a wavelength of 514.5 nm, a scanning speed of 40 mW, and a girder beam of 2 μm.

4.2 S isotopes

The S isotope ratios are provided as $\delta^{34}S$ relative to the Canyon Diablo troilite, and the analytical repeatability is ±0.2‰ (Mao et al., 2008). For the sulfur isotopic analysis, 12 sulfide samples from ores and veins with sulfides at various phases of mineralization were chosen. The Sulfur Isotope Center at the Department of Mineral Reserves, Chinese Ministry of Geosciences, Beijing, harnessed a Finnegan MAT-251EM atomic absorption spectrophotometer. Compared to Caón Diablo Troilite (CDT), the amount of sulfur isotopes is in per mil (‰) units. The accuracy of this method can within ±0.2‰. At the MLR Central Research Lab of Mineral deposits and Mineral Characterization, CAGS, measurements took place using the MAT251EM spectrometer. This analytical method is consistent with Duan et al. (2010). The analytical reproducibility was ±0.2‰, and the proportion of the S element to the black meteorites in the canyon was $\delta^{34}S$ (Mao et al., 2008).

4.3 Pb isotopes

For galena isotopic analyses, 16 samples including 12 sulfides and four granitoid rocks were selected. Thermoelectric ablation

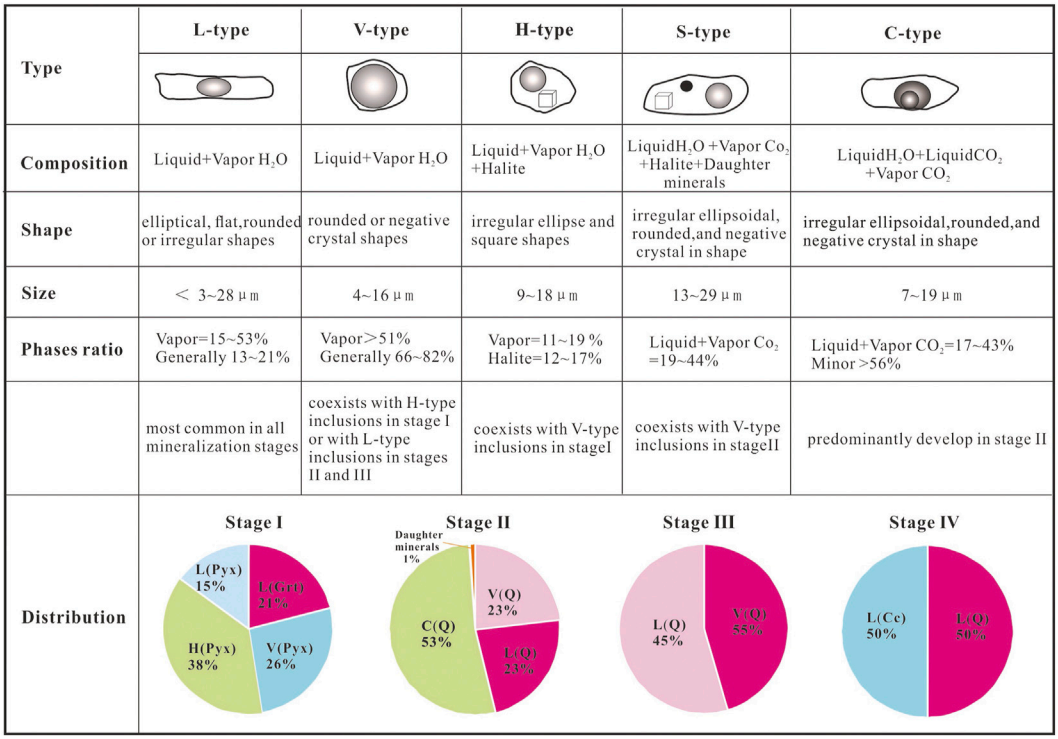

FIGURE 6
Characteristics and distributions of fluid inclusions in the Shibaogou Mo–Pb–Zn deposit.

absorption spectroscopy by ISOPROBE-T was used to revise the feldspars in the datasets. Galena isotope compositions are analyzed using a Phoenix thermo desorption Raman spectroscopy with a single band, M^+, and an adjustable multi-Faraday receiver. When the vacuum in the analysis chamber is less than 2.0E-8 mbar, take measurements. Sweep the peak to modify the focusing parameters and control the intensity of the highest abundant isotope ion current to achieve 1×10^{-11}. For measurement after heating to an appropriate temperature, NBS981s standard sample data is $^{208}Pb/^{206}Pb$ = 2.1673–2.1689, $^{207}Pb/^{206}Pb$ = 0.91431–0.91497, and $^{204}Pb/^{206}Pb$ = 0.059005–0.059079, with a background Pb of 100 pg during the entire process.

4.4 H–O isotopes

Shibaogou granite metamorphic rock and carbonate's contact area possessed skarn minerals which been probed. This article assessed the quartz in columns representing lamellar molybdenite. Moreover, two kinds of quartz, galena and sphalerite, were isolated in quartz veins in this test. In the later stages of quartz veins and calcite deposits, a total of two calcites are obtained. A CAGS Mineralogical composition Organization MAT253EM spectrometer was deployed to scan minerals. The monitoring and estimation approach devised by Zhang, (2014) was verified through inspection of H and O isotopes, and the determination accuracy of the O isotope is greater than ±0.1‰, while that of the H isotopic element is above ±0.1‰ (Mao et al., 2008). The Beijing Bureau of Mineral Resources' carbon isotope treatment center undertook modeling and simulation on the isotopic of both hydrogen and oxygen. Before water was extracted from the 40–80 mg rock isolation solution, the specimens were divided *via* magnetic tape extraction processes and hand diagnostic tests. Then, at a high temperature of 600°C, the liquid is separated from the liquid. Before performing the D/H test, measure the exhaust gas with a pressure gauge. In the $^{18}O/^{16}O$ analysis, 1 mg of oxygenates were treated with laser-heated chlorine trifluoride (Macaulay et al., 2000) and his men. Similar to Fallick et al. (1993), the oxygen isotope laser fluorination process was discussed, which described the hydrogen isotopes. For $\delta^{18}O$ and δD tests, the accuracy determined by repeated analysis was ±0.2‰. At the assumed crystallization temperature, the isotopic composition of the fluids studied in the study was determined using appropriate fractionation factors (Table 1). The compositions of oxygen and hydrogen isotopes are stated in ‰ terms of Vienna Standard Mean Ocean Water (V_{-SMOW}).

TABLE 1 Summary of microthermometric data fluid inclusions from the Shibaogou Mo–Pb–Zn deposit.

Stage	Type[a]	Host mineral	Tm, ice (°C)[b]	Tm, CO_2 (°C)[c]	Tm, cla (°C)[d]	Th, CO_2 (°C)[e]	Tm, halite (°C)[f]	Th, total (°C)[g]	Peak of Th	Salinity (wt%)
I	L	Grt	−10.9 ~ −6.2					453 ~ >550	500–550	9.47–14.94
		Pyx	−6.0 ~ −0.3					357–432		0.53–9.21
	V	Pyx	−3.5 ~ −0.2					513–550		0.35–5.7
	H	Pyx					264–387	413–562		35.58–46.05
II	L	Qtz	3–8.2					256–397	350–400	3.57–11.97
	V	Qtz	8.6–9.7					314–397		0.62–2.81
	C_1	Qtz	5.2–9.8		−59.4 ~ −57.1			324–387		0.41–8.77
III	L	Qtz	−5.8 ~ −0.5					163–347	200–250	0.87–8.94
	V	Qtz	−5.7 ~ −1					303–347		1.73–8.81
IV	L	Qtz	−14 ~ −0.8					103–247		0.88–11.34
		Cc	−3 ~ −0.2					151–231		2.07–8.41

[a]Fluid inclusion type: L = liquid-rich; V = vapor-rich; H = halite-bearing; C_1 = CO_2-bearing two-phase; C_2 = CO_2-bearing three phase.
[b]Tm, ice: final ice melting temperature.
[c]Tm, CO_2: final solid CO_2 melting temperature.
[d]Tm, cla: final CO_2 clathrate dissociation temperature.
[e]Th, CO_2: CO_2 phase homogenization temperature.
[f]Tm, halite: halite dissociation temperature.
[g]Th, total: total homogenization temperature.

TABLE 2 Molybdenite Re-Os dating results of the Shibaogou Mo–Pb–Zn deposit.

Sample	Weight (g)	Re (μg/g)		Os (ng/g)		^{187}Re (μg/g)		^{187}Os (ng/g)		Model age (Ma)	
		Value	2σ	Value	2σ	Value	2σ	Value	2σ	Value	2σ
710–10	0.02089	3.9163	0.0353	0.3938	0.0542	2.4614	0.0222	62.09	0.37	151.2	2.2
710–10	0.03049	2.5258	0.0233	2.9949	0.0279	1.5875	0.0146	39.67	0.29	149.8	2.3
710–15	0.01000	2.9130	0.0255	0.2141	0.0495	1.8309	0.0160	45.32	0.33	148.4	2.2
710–7	0.02034	1.7848	0.0132	0.0224	0.0405	1.1218	0.0083	27.76	0.17	148.4	2.0
Sbj710-1	0.03022	5.2229	0.0719	0.0204	0.0078	3.2827	0.0452	80.09	0.46	146.3	2.6
710–20	0.03128	4.4319	0.0558	0.2950	0.0083	2.7855	0.0350	69.24	0.40	149.0	2.5

4.5 Molybdenite Re-Os dating

A total of seven molybdenites with a weight >300 μg, a purity >93% and a particle size of less than 0.2 mm were determined from samples taken at 20-m intervals down the shibaogou mine. Our sampling can reduce the coupling consequence of Re and Os, resulting in higher accuracy (Stein et al., 2003). The TJA-X series ICP-MS apparatus, National Geographical Analysis and Research Center, Chinese Academies of Geosciences, was harnessed in accordance with the analytical procedure described by (Du et al., 2001) The molybdenite age was calculated to be model years (Smoliar et al., 1996). The model age of molybdenite was estimated.

5 Results

5.1 Molybdenite Re-Os dating

The Re-Os data of six molybdenite samples collected at intervals of 20 m from the Shibaogou mine are shown in Table 2. The content of ^{187}Re was 11.218–32.827 μg/g with an average value of 21.783 μg/g, and the content of ^{187}Os was in the range of 27.76–80.09 ng/g with an average value of 54.03 ng/g. Re-Os model ages ranged from 146.3 to 151.2 Ma, with a weighted mean age of 148.9 ± 1.7 Ma. The ^{187}Re-^{187}Os isochronous age is 147.4 ± 7.2 Ma. All age values were processed and obtained using ISOPLOT software (Ludwig, 2003) and are similar to model age.

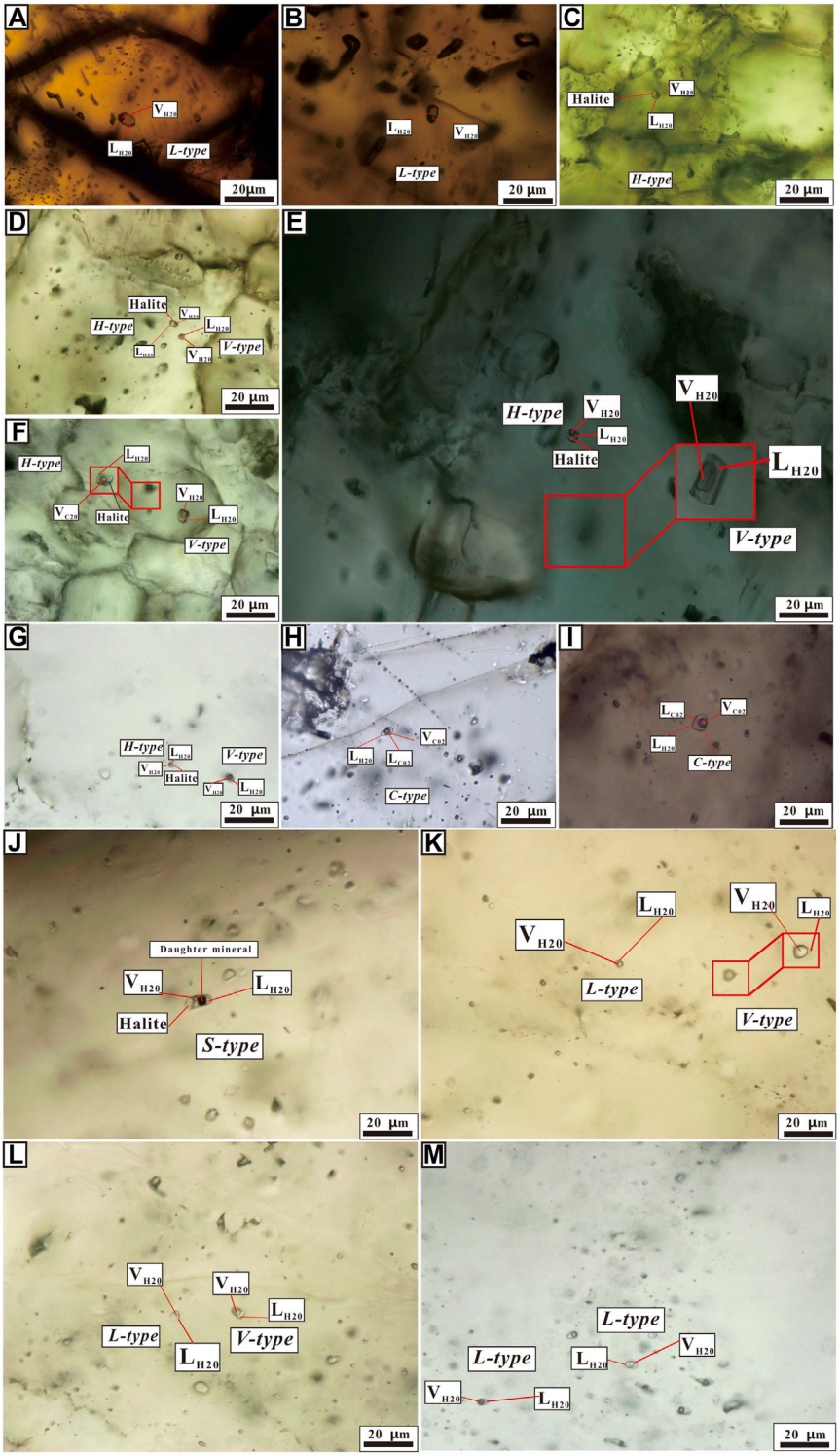

FIGURE 7
Photomicrographs of representative fluid inclusions (fluid influsions) of different types in the Shibaogou W (Mo) deposit. **(A)** Liquid-rich (L-type) fluid inclusions in garnet; **(B)** liquid-rich (L-type) fluid inclusions in garnet; **(C)** halite-bearing/hypersaline (H-type) fluid influsions in pyroxene; **(D)** halite-bearing/hypersaline (H-type) fluid influsions in pyroxene; **(E)** coexisting vapor-rich (V-type) inclusion and halite-bearing/hypersaline (H-type) inclusion in pyroxene; **(F)** coexisting V-type fluid inclusions and L-type fluid inclusions hosting a quartz crystal in stage I pyroxene; **(G)** coexisting vapor-rich (V-type) inclusion and halite-bearing hypersaline (H-type) inclusion in pyroxen; **(H)** CO_2-bearing three phase inclusions (C-type) in stage II quart; **(I)** CO_2-bearing three phase inclusions (C-type) in stage II quart; **(J)** S-type inclusion in stage II quart; **(K)** L-type and V-type fluid influsions in stage III quartz; **(L)** L-type fluid influsions in stage IV calcite; and **(M)** L-type fluid influsions in stage IV calcite.

5.2 Fluid inclusion

Based on the classification principles (Roedder 1984; Lu et al., 2004), primary fluid inclusions in garnet and pyroxene from the first stage, quartz from the second and third stages, and calcite from the fourth stage at room temperature are observed. The Shibaogou deposit has fluid inclusions of five distinct types (Figures 6, 7).

The L-type fluid inclusions consist of a 10–50 vol% vapor phase (V_{H2O}) and a liquid phase (L_{H2O}) at air conditions. From stage I through stage IV, L-type fluid influsions are most prevalent. L-type fluid inclusions frequently range in size from 2 to 30 μm. Oval, flat, or circular fluid inclusions help compensate the L-type (Figures 7A,B,M).

The V-type fluid inclusions can be found a larger vapor ratio. At ambient temperature, the additions' darkly colored bubbles represent more than half of the total volume (Figures 7C,D). The size of V-type fluid inclusions is about 5–15 μm, and the shapes are mostly oval, triangular, and irregular. Now at sedimentary deposits stage (Figures 7C,D), they mix with H-type fluid inclusions, and at the II and III phases in quartz, they cohabit with L-type fluid inclusions (Figures 7D–F).

The C-type fluid inclusions are characterized by coexisting three phases includingV_{CO2} phases, L_{CO2} phases and L_{H2O} phases (Figures 7H,I). The V_{CO2} and L_{CO2} phases occupy 35%–70% of the total inclusion volume. The fluid inclusions of the C-type variation are elliptic, round, and also have deformed crystalline structure. The C-type fluid inclusions spanned around 8–20 μm in size which have predominantly developed in stages II and very few in stage III.

The H-type fluid inclusions contain three phases including L_{H2O} phases, V_{H2O} phases and halite phases. The H-type fluid inclusions are negative crystal shapes with 9–18 μm in size (Figures 7D–F). In phases II, there are very few pyroxene and quartz crystals, but in the sedimentary deposits stage, these grains are valuable international with V-type fluid inclusions. The H-type fluid influsions are significantly neglected in the Shibaogou deposit in contrast to other types of fluid influsions. Furthermore, this species of fluid influsions is homogenized by burst departure following the slow breakdown of cubic halite (Figure 7G).

The S-type fluid inclusions contain three phases including L_{H2O} phases, V_{H2O} phases, halite phases and stages of daughter elements. The S-type fluid inclusions are mainly negative crystal shapes. The S-type fluid inclusions are 10–20 μm in size (Figures 7D,J). The S-type fluid inclusions are much less observed than other liquid inclusions types but are mainly found in quartz grains in stages II. The S-type liquid inclusions are homogenization by bubble disappearance after cubic halite gradually dissolution but daughter minerals are not homogenized.

5.2.1 Microthermometry

The microthermometric data were collected from isolated inclusions in transparent mineral from stage I to stage IV excluding those secondary inclusions which have necking or leaking features. The results of fluid inclusion salinity and homogenization temperature from different mineralization stages are summarized in (Table 1; Figure 7) and the following paragraphs.

1) In the skarn stage, the pyroxene minerals are characterized by predominant H-type, L-type, and V-type fluid inclusions, and garnet grains host numerous L-type and minor V-type fluid inclusions (Figures 7D–F). In garnet, the median temperature of L-type fluid influsions is between 453 and 550°C, between −10.9 and −6.2°C, and between 9.47 and 14.94 wt% NaCl equiv. (Table 1 and Figures 7A,B). In contrast, the augite minerals of L-type fluid influsions are between 357 and 432°C, −6.0~−0.3°C, and 0.53 wt%–9.21 wt% NaCl equiv. (Table 1 and Figures 8A,B). Nevertheless, H-type fluid influsions are still detectable in pyroxene, and even when the rock ice melts, the liquid water in these clathrates remains persistent. The H-type fluid influsions had salinity levels of 35.58 wt%–46.05 wt% NaCl equiv, a mean temperature of 413–562°C, and a soluble of rock salt of 264–387°C (Table 1 and Figures 7D–F). The results demonstrate that 513–550°C is the ultimate homogenized temperature of V-type fluid influsions in pyroxene.
2) In the quartz–molybdenite stage, homogeneity heats, and eventual glacial melt temperatures of the L-type fluid influsions in the quartz–molybdenite vein are 256–397°C, −3~ −8.2°C, 3.57 wt%–11.97 wt% (NaCl equiv.). Alternating V-type fluid inclusions and L-type fluid inclusions (Figure 7K), with salt concentrations that varied (0.62–2.81 and 3.57 wt%–11.97 wt% NaCl equiv., separately), and homogenized temperatures and is equivalent (314–397°C and 256–397°C, correspondingly; Table 1). C-type fluid inclusions were homogenized in 0.41 wt%–8.77 wt% NaCl equiv in the range of 324–387°C. In addition, there is an S-type inclusion that yielded a homogenization temperature of 381°C (Figure 9C).
3) In the quartz–galena–sphalerite stage, the predominant L-type fluid influsions in quartz grains possess homogenized temperatures between 163 and 347°C and final glacial melt temperatures between −5.8 and −0.5°C, with salinities ranging from 0.8 wt% to 7.94 wt% NaCl equivalent. The temperature measurement in the V-type fluid influsions in quartz ranges from 1.73 wt% to 8.81 wt % NaCl equiv., 173–347°C for homogeneity, and −5.7 to −1°C for terminal ice melting, respectively. (Table 1 and Figures 7L, 9E,F).
4) In the carbonate stage, considering homogenized temperatures of 151–231°C, eventual melting ice

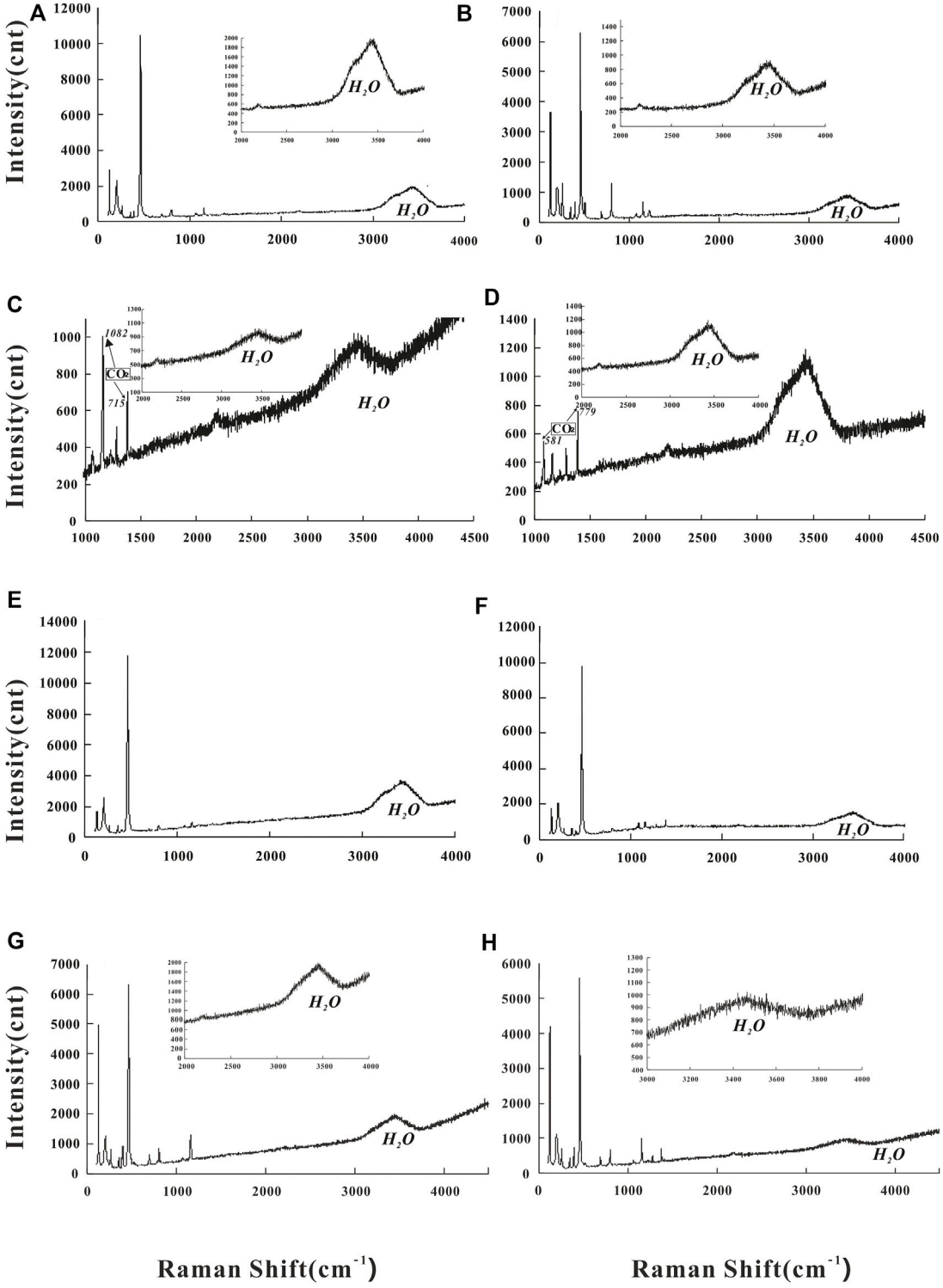

FIGURE 8
Representative laser Raman spectra for fluid inclusions from the Shibaogou Mo–Pb–Zn deposit. **(A)** H-type fluid inclusion in the anhydrous skarn stage I; **(B)** L-type fluid inclusion in the hydrous skarn stage I; **(C)** C-type fluid inclusion in the quartz–molybdenite stage II; **(D)** C-type and L-type fluid inclusion in the quartz–sulfide stage II; **(E,F)** L-type fluid inclusion in the quartz–galena–sphalerite stage III; **(F)** L-type fluid inclusion in the carbonate stage IV; and **(G,H)** L-type fluid inclusion in the carbonate stage IV.

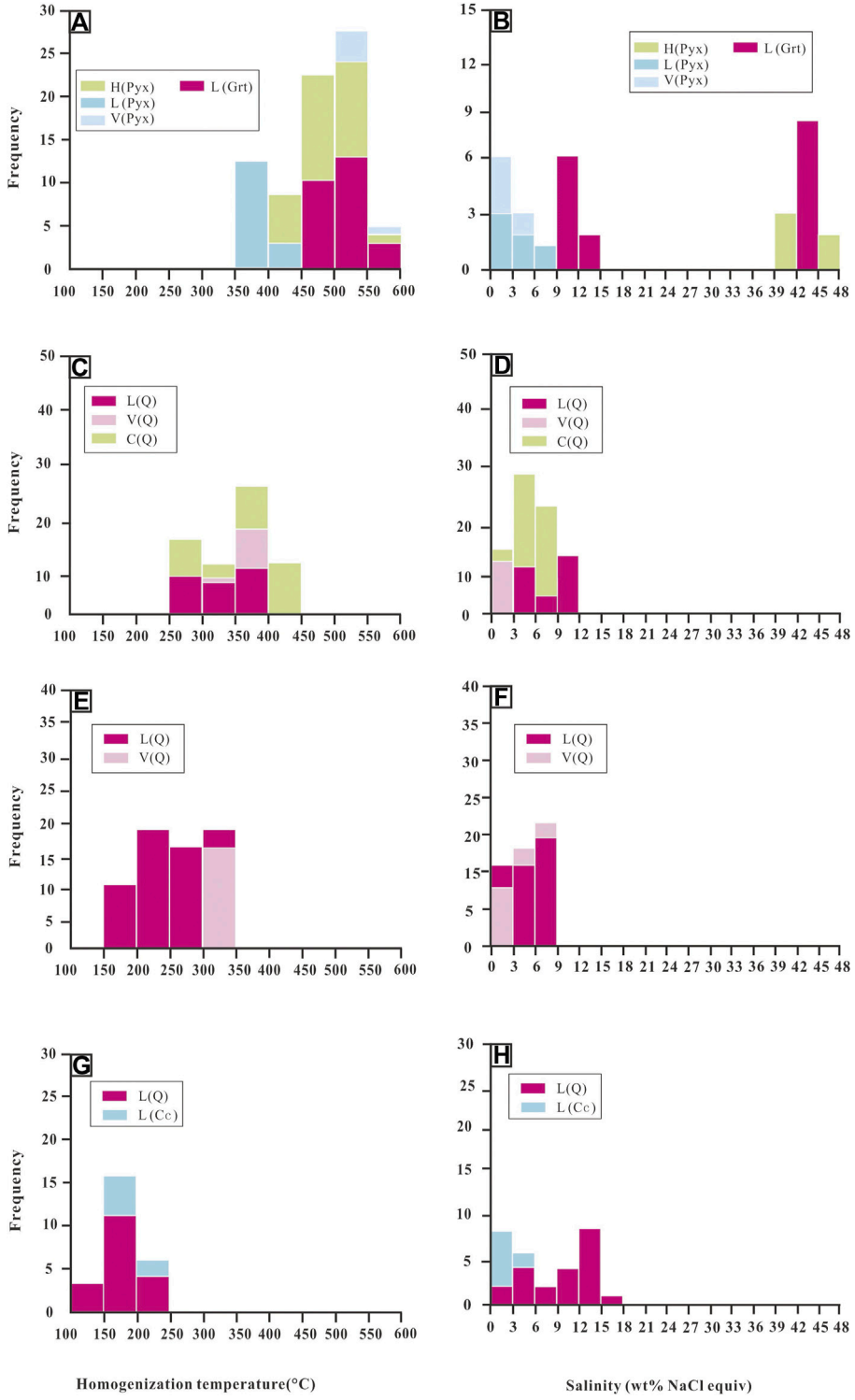

FIGURE 9
Histograms of homogenization temperatures and salinities for all inclusion types in the Shibaogou Mo–Pb–Zn deposit; **(A,B)** variations of homogenization temperatures and salinities in the anhydrous skarn stage; **(C,D)** variations of homogenization temperatures and salinities in the hydrous skarn stage; **(E,F)** variations of homogenization temperatures and salinities in the quartz–sulfide stage; and **(G,H)** variations of homogenization temperatures and salinities in the carbonate stage.

TABLE 3 H–O isotope data of garnet, scheelite, and quartz from the Shibaogou Mo–Pb–Zn deposit.

Stage	Sample	Mineral	$\delta^{18}O_{SMOW}$ (%)	$\delta^{18}O_{fluid}$ (%)	δD_{SMOW} (%)	δD_{SMOW} (%)
I	65–1	Garnet	5.9	4.163	−79.9	−79.9
	65–2	Garnet	6	4.288	−83.3	−83.3
II	710–1	Quartz	14.5	8.997	−98.2	−98.2
	710–10	Quartz	10.8	6.325	−91.8	−91.8
III	710–20	Quartz	10.3	1.809	−105.4	−105.4
	710–16	Quartz	11.5	3.009	−104.3	−104.3
IV	710–6	Quartz	12.2	−1.768	−102.7	−102.7
	710–19	Quartz	12.8	−1.168	−106.5	−106.5

Isotope fractionation equilibrium formulas used in the following mineral-water system (Kelvin for T), including (1) garnet–water (Taylor, 1974), (2) scheelite-water (Wesolowski and Ohmoto, 1986), and quartz–water (Clayton et al., 1972).

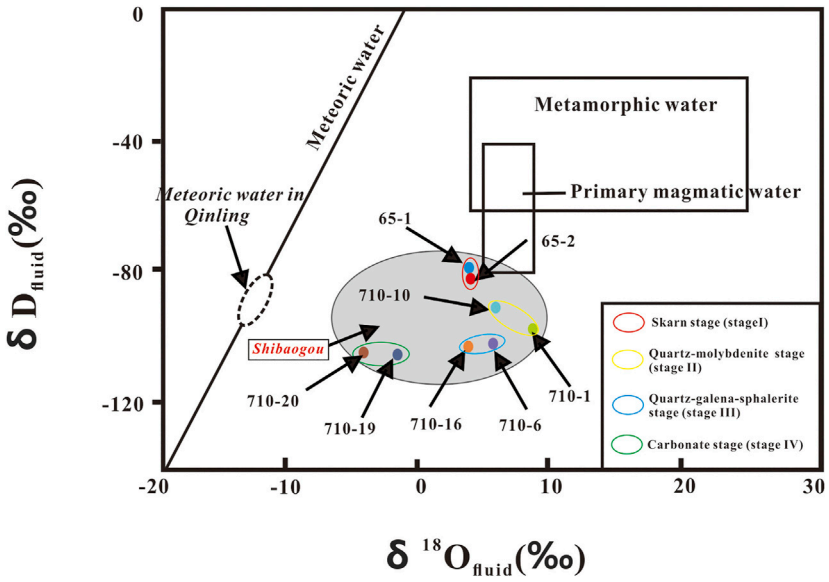

FIGURE 10
The $\delta^{18}O_{fluid}$ vs. δD_{fluid} diagram of the Shibaogou Mo–Pb–Zn deposit.

temperatures of −3 to −0.2°C, and salt concentrations ranging from 2.07 wt% to 8.41 wt% NaCl equiv, calcite minerals include a rich source of L-type fluid influsions (Table 1 and Figure 9H). The L-type fluid influsions also predominate in quartz, with homogenized temperatures ranging from 130 to 249°C, utmost ice melting temperatures of −14 to −0.8°C, and high salinity from 0.88 wt% to 11.34 wt% NaCl equiv (Figures 9G,H).

5.2.2 Laser Raman spectroscopy

In order to restrict the gas–liquid two-phase components in the liquid inclusions, Laser Raman spectroscopy was performed to identify the fluid inclusions from all stages. H_2O–NaCl appears to be the predominant constituent of the flow in the sedimentary deposits stage (I) since it is present in both the liquid and gas phases of the H-type inclusions in the pyroxene crystals (Figure 8A). The solvent phase and gasoline phase of the predominant C-type clathrate of quartz (quartz–molybdenite stage) are close to CO_2 (Figures 8C,D), indicating that the components of the quartz–molybdenite section are H_2O–NaCl–CO_2 (stage II).

The gas phase and liquid phase components of the L-shaped aggregates inside the quartz–galena–sphalerite stage and carbonate stage (stage IV) were confirmed only in H_2O, lacking CO_2, indicating the feature of the H_2O–NaCl system (Figures 8E–H).

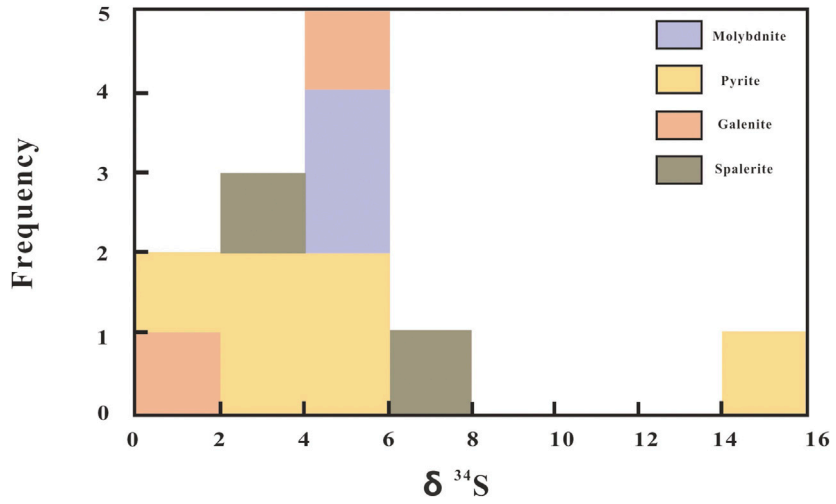

FIGURE 11
Histogram of sulfur isotope values of sulfide minerals in the Shibaogou Mo–Pb–Zn deposit.

TABLE 4 Pb isotope data and S isotope composition of sulfides from the Shibaogou deposit.

Sample	Mineral	$\delta^{34}S$ (‰)	$^{206}Pb/^{204}Pb$	$^{207}Pb/^{204}Pb$	$^{208}Pb/^{204}Pb$
710–1	Galenite	5.1	17.541	15.457	38.549
710–19		0.8	17.644	15.503	38.449
710–1	Sphalerite	6.3	17.571	15.497	38.675
710–19		2.4	17.678	15.534	38.575
710–1	Pyrite	5.7	17.557	15.505	38.69
710–6		4.1	17.383	15.508	38.432
710–10		3.4	17.383	15.499	38.366
710–19		2.3	17.67	15.538	38.575
710–7	Molybdenite	14.7	18.037	15.592	38.834
710–16		1.9	17.654	15.524	38.616
710–20		5.1	17.53	15.442	38.371
sbg858-2		5.9	17.589	15.458	38.365
716–1	Granite		17.696	15.468	38.553
716–2			18.064	15.473	38.631
868–1			18.741	15.510	38.592
858–4			17.826	15.463	38.742

5.3 H–O–S–Pb isotopes

Table 3 and Figure 10 including information on the hydrogen and oxygen isotopic in garnet, quartz, and calcite from stage I to stage IV of the Shibaogou Mo–Pb–Zn deposit. The solution absorption temperature is employed to quantify all hydrogen and oxygen isotopes. The hydrogen as well as oxygen isotopic proportions of two garnets from Skarn are $\delta^{18}O_{fluid}$ = 4.163‰–4.288‰ (averaging 4.25‰) and δD_{fluid} = −79.9‰ to −83.3‰ (averaging −81.6‰). In the quartz–molybdenite stage, the oxygen isotope ($\delta^{18}O_{fluid}$) values were obtained for two quartz samples (6.325‰–8.997‰, with a mean of 7.6‰). Hydrogen isotope in quartz samples was from −98.2% to −91.8‰ (averaging −95‰).

In the quartz–galena–sphalerite stage, the $\delta^{18}O_{fluid}$ and δD_{fluid} measurements from two quartz extracts were 1.8‰–3.4‰ (median 2.6‰), and −95.7‰ to −85.2‰ (averaging −90.45‰), correspondingly. The hydrogen and

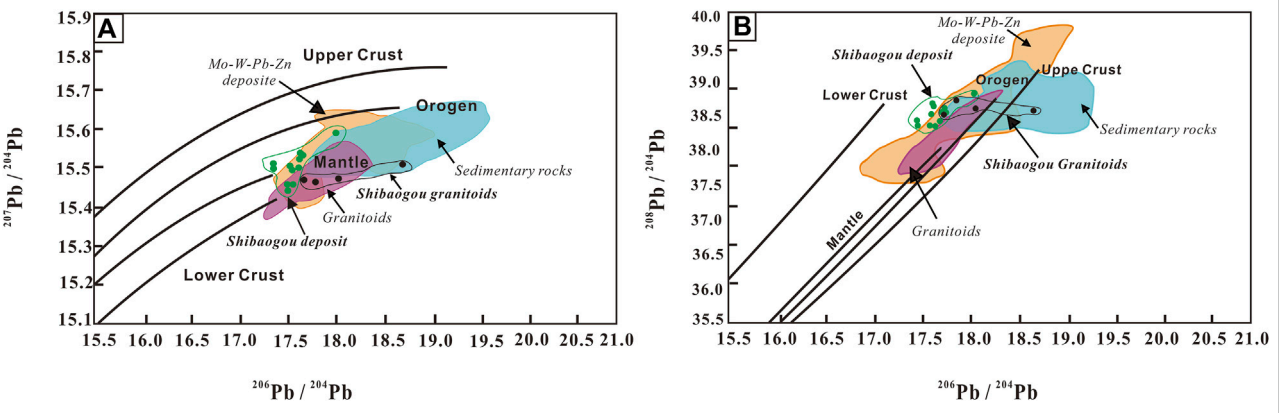

FIGURE 12
Plot of $^{207}pb/^{204}pb$ vs. $^{206}pb/^{204}pb$ **(A)** and $^{208}pb/^{204}pb$ vs. $^{206}pb/^{204}pb$ **(B)** for the Shibaogou sulfides, local granitoids, and host rocks. Pb isotope compositions of sulfides in the Shibaogou deposit. Pb isotope compositions in the Mo–W–Pb–Zn deposits of the Luanchuan ore district are after Huang et al., 1984; Luo et al., 1991; Yan, 2004; Qi, 2006; Yan et al., 2009; Duan et al., 2011; Cao et al., 2015; Yang et al., 2017. Pb isotope compositions causative granitoids are cited from Huang et al., 1984; Luo et al., 1991; Guo, 2018. Galena isotope values of sedimentary rocks are from Liu et al., 2007; Yan et al., 2009.

oxygen isotopes compositions of two calcite samples in the quartz–calcite stage are $\delta^{18}O_{fluid}$ = −1.769‰ to −1.168‰ (averaging −1.46‰) and δD_{fluid} = −106.5‰ to −102.7‰ (averaging −104.6‰).

Figure 11 as well as Table 4 both display the conclusions of the measurement of 12 sulfides' sulfur isotopes from the Shibaogou molybdenum deposit. The $\delta^{34}S$ values of three molybdenite samples are between 1.9‰ and 14.7‰, and four pyrite samples are 2.3‰–5.7‰, two sphalerite specimen range from 2.4‰ to 6.3‰, and two galena samples are 0.8‰–5.1‰.

Four molybdenite samples host Pb isotope $^{206}Pb/^{204}Pb$ = 17.53–18.037, $^{207}Pb/^{204}Pb$ = 15.442–15.592, and $^{208}Pb/^{204}Pb$ = 38.365–38.834. Four pyrite samples have $^{206}Pb/^{204}Pb$ ratios of 17.383–17.67, $^{207}Pb/^{204}Pb$ ratios of 15.499–15.538, and $^{208}Pb/^{204}Pb$ ratios of 38.366–38.69. Two sphalerite samples have $^{206}Pb/^{204}Pb$ ratios of 17.571–17.678, $^{207}Pb/^{204}Pb$ ratios of 15.497–15.534, and $^{208}Pb/^{204}Pb$ ratios of 38.575–38.675. Two galena samples have $^{206}Pb/^{204}Pb$ ratios of 17.541–17.644, $^{207}Pb/^{204}Pb$ ratios of 15.457–15.503, and 208Pb/^{204}Pb ratios of 38.449–38.549. Four granite samples have $^{206}Pb/^{204}Pb$ ratios of 17.696–18.741, $^{207}Pb/^{204}Pb$ ratios of 15.463–15.510, and $^{208}Pb/^{204}Pb$ ratios of 38.553–38.742 (Table 4; Figure 12).

6 Discussion

6.1 Age of skarn Mo mineralization

Because the Re-Os isotope system is relatively closed, the influence of later transformation is small, and the metallogenic age of the deposit can be directly and accurately determined (Suzuki et al., 1996; Stein et al., 2001). In this study, the Re-Os isochron age and the model age-weighted average age of molybdenite in contact zone are 147.4 ± 7.2 Ma and 148.9 ± 1.7 Ma, respectively, which represents the age of the mineralization in the Shibaogou Mo deposit. The metallogenic age is identical to the zircon U–Pb ages of the Shibaogou granitic intrusions (148 ± Ma, Xue et al., 2018), which indicates the mineralization of the Shibaogou Mo deposit is genetically relevant to the Shibaogou granites.

In the EQOB, there are multiple Mo mineralization events from Late Paleoproterozoic to Late Cretaceous including Late Paleoproterozoic to Early 1875–1686 Ma, ~429 Ma, 233–210 Ma, 156–132 Ma, and 128–107 Ma revealing the complicated tectonic evolution of the Qinling orogenic belt (Li et al., 2009, 2011; Wei et al., 2009; Deng et al., 2013). Our brand molybdenite Re-Os dating results demonstrate that the Shibaogou skarn Mo deposit also belongs to the Early Yanshanian episodes of Mo mineralization similar to some porphyry and skarn-porphyry Mo deposits in the LOD indicating the possible post-collisional extension between the NCC and Yangtze Craton and the subduction of the Paleo-Pacific Plate during the Early Cretaceous in the EQOB (Yang et al., 2019).

6.2 Source of the ore-forming fluids by H–O isotopes and materials by S–Pb isotopes

The Hydrogen and oxygen isotopes compositions of minerals from the deposit are widely used to trace the sources of mineralizing fluids and materials (Hedenquist and Lowenstern, 1994; Meinert et al., 2005; Peng et al., 2016). Garnet in the skarn stage shows relatively high and a narrow range of $\delta^{18}O_{fluid}$ values (5.9‰–6‰) which is similar to the other skarn deposits in the world (Meinert

et al., 2003; Kodõera et al., 2010; Peng et al., 2016; Lei et al., 2018; Li et al., 2020) and maybe indicate the magmatic origin (5.0‰–9.0‰; Hugh and Taylor, 1974; Hedenquist and Lowenstern, 1994). Furthermore, the $\delta^{18}O_{fluid}$ values of the quartz minerals from the quartz–molybdenite stage is a narrow range (6.3‰–8.9‰), which are similar to the values of magmatic water (Figure 10), it shows the characteristics of a magma. In the quartz–galena–sphalerite stage, the values of $\delta^{18}O_{fluid}$ (1.8‰–3.0‰) are lower than values in the quartz–molybdenite stage but still close to the magmatic water which may be caused by the meteoric water. But, the δD_{H2O} values in all stages (−106.5‰ to −79.9‰) are lower than the values of magmatic water (Figure 10), and it maybe the product of open-system degassing of parental magm (Hedenquist and Richards, 1998; Peng et al., 2016; Yang et al., 2020).

The values of $\delta^{18}O_{fluid}$ in the quartz–molybdenite and quartz–galena–sphalerite stages are higher than in the skarn stage which may be achieved *via* the mineral precipitation from a boiling solution (Lynch et al., 1990; Bowers, 1991), or a result of interactions between magmatic fluids and surrounding carbonate rocks (Hoefs, 2009; Catchpole et al., 2015). However, the boiling occurring in fluids of the syn-ore stage could not have been responsible for the >10‰ increase in the $\delta^{18}O_{fluid}$ value of the fluids (Peng et al., 2016). Thus, the elevated $\delta^{18}O_{fluid}$ values in syn-ore-stage minerals are mainly contributed by the fluid–rock interactions between the magmatic fluid and the surrounding carbonate rocks. At first, the $\delta^{18}O_{fluid}$ values of the calcites from the post-ore-stage vein are lower than in quartz–galena–sphalerite stage minerals, further suggesting the termination of the fluid–rock interactions between the magmatic fluid and the surrounding carbonate rocks. In addition, the values of $\delta^{18}O_{smow}$ in the Shibaogou Mo deposit are consistent with the $\delta^{18}O_{smow}$ values of the carbonate rocks from the Luanchuan group, indicating the fluid–rock interactions (Table 3).

The lack of sulfate minerals indicates that ore-forming fluids are mainly H_2S, as well as low $f(O_2)$ and pH (Duan et al., 2010). Besides, the variations of $\delta^{34}S$ values in the Shibaogou Mo deposit conform to the fractionation sequence molybdenite > pyrite > sphalerite > galena (Zheng, 1990), revealing that they were in equilibrium during ore deposition (Figure 11). In a word, the values of the $\delta^{34}S$ composition for the sulfides from Shibaogou Mo deposit can show the S isotopic composition of the ore-forming fluids. At the Shibaogou Mo deposit, the $\delta^{34}S$ values of sulfide minerals exhibit a narrow range of 1.9‰–6.3‰ (only one exceptional value of 14.3‰ from pyrite) indicating a homogeneous sulfur source. Similar to the H–O isotopes, the $\delta^{34}S$ values in the Shibaogou Mo deposit are similar to the values of typical skarn deposits throughout the world (Soloviev and Kryazhev, 2018a; 2018b; Lei et al., 2018; Xue et al., 2018; Soloviev et al., 2019; Wang et al., 2019), indicating the major magmatic source with some contributions from sedimentary rocks. The Pb isotopes were also used here to constrain the source ore materials. The similarities between the ores and the Shibaogou granites suggest the ore-forming materials originated from the magmas which formed the Shibaogou granites. As shown in (Figure 12), the sample points plot in the domain between the orogen and the mantle, the lower crust, and the mantle, respectively implying the mixing sources of crust and mantle in general. Previous studies have proven the assignable role of mantle materials in the generations of granites and deposits in the LOD (Richards, 2009; Richards, 2011; Wang et al., 2015; Yang et al., 2016; Xu et al., 2021).

In conclusion, the source of the ore-forming fluids were the fluid–rock interactions between the magmatic fluid and the surrounding carbonate rocks, and the ore-forming metal materials were camed from the magmas which generated the Luanchuan granites having a mixing source of crust and mantle.

6.3 Evolution of the ore-forming fluids

By studying the properties of primary fluids, we can further understand the evolution of fluids in the process of mineralization (Roedder, 1984). Modification of fluid inclusions after entrapment may confuse their interpretation (AudeAtat and Günther, 1999) through changes in bulk density and/or composition (Roedder, 1984; Bakker and Jansen, 1994; AudeAtat and Günther, 1999). In this study, features such as decrepitation halos, movement tracks, stretching or shrinkage, and extremely irregular inclusions were therefore avoided.

As shown by this study, the ore-forming fluids are moderate to high salinities (35.58 wt%–46.05 wt% NaCl equiv.) and high homogenization temperatures of 513–550°C, similar to those in typical skarn deposits (Bao et al., 2014; Cao et al., 2015; Xue et al., 2018). In pyroxene, H-type inclusions and V-type inclusions coexist (Figures 7D–F). They have similar temperature but different salinity (Figures 9A,B), indicating that fluid boiling occurs during the mineralization process (Roedder and Bodnar, 1980). Therefore, through the study of boiling inclusions, we can calculate the accurate trapping pressure and infer the mineralization depth. The Fls of the deposit could have been formed at 580–650 bar estimated by the isobar equations (Figure 13A), and the lithostatic depth of the region is between 2.19 and 2.45 km, which is similar with the emplacement depth of the Shibaogou granite porphyry (1.49–3.99 km; Xue et al., 2018). Moreover, the primary L-type fluid inclusions trapped in pyroxenes are homogenized by sudden vapor disappearance instead of gradual disappearance or expansion could represent the initial single-phase supercritical fluid derived from a magmatic–hydrothermal system (Veksler, 2004; Zajacz et al., 2008). Thus, the fluid with a salinity of 6 wt%–8 wt% NaCl equiv. is an initially supercritical exsolved from the Shibaogou intrusion (Hedenquist and Lowenstern, 1994; Shu et al., 2013). When the fluid continued to rise along the structural fissure to a depth of 2.19–2.45 km, the exsolved fluid intersected

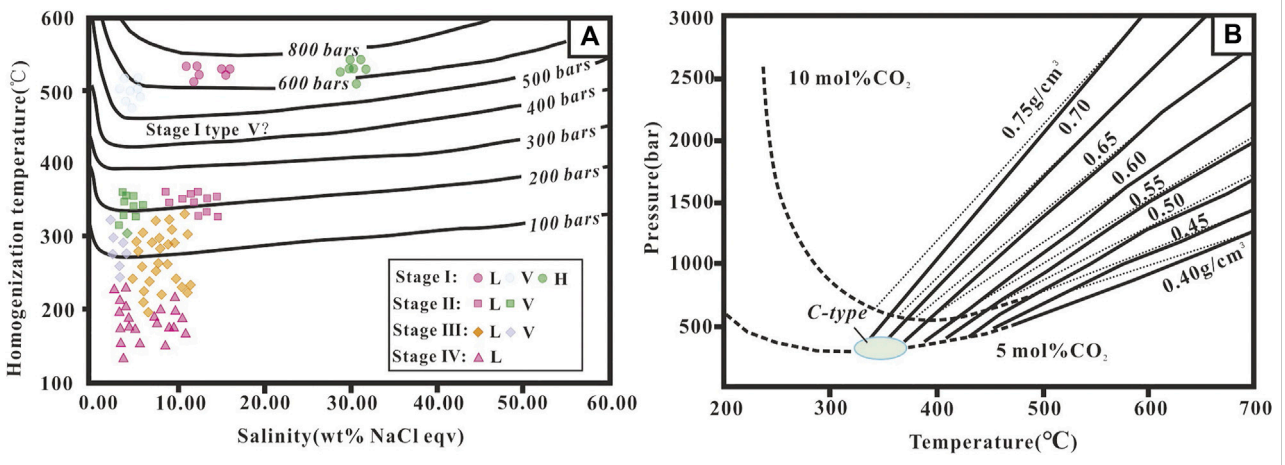

FIGURE 13
Pressure estimation for ore stage I to IV fluid inclusions. **(A)** Fluid inclusion assemblages from stages I to III were trapped under boiling conditions, and isobar was calculated from the equations of Driesner and Heinrich (2007). **(B)** Isochrones for fluid of 4 wt% NaCl, 5 mol% CO_2 and 10 mol% CO_2. The solid lines mark the solvi for fluids in the system H_2O (6 wt%)–NaCl–CO_2 (5–10 mol% CO_2; Gehrig et al., 1986). Data for the C-type fluid inclusions plot in the oval field, indicating trapping pressures of <500 bar.

the solution to form two fluids with different properties, high-salinity and low-salinity fluids (path 1 in Figure 14).

Comparatively, the mineralizing fluids have characteristics of moderate temperatures (256–397°C) and salinities (3.57 wt%–11.97 wt% NaCl equiv.) in stage (II). Some authors suggested that such changes in fluid properties can be caused by gradual mixing with atmospheric water, but the isotopic results have proven the insignificant role of the meteoric water and the dominance of magmatic water in this stage (Figure 10). As the magma cools and crystallizes, the upwelling fluid no longer intersects the two-phase surface due to the lack of power and heat from the magma (Shinohara and Hedenquist, 1997). However, we found a large number of dykes (Figure 4I) in the ore body, which provided heat to the upwelling fluids, which caused the ore-forming fluids to intersect again with the two-phase surface to form two fluids with different properties, medium-to-high-salinity and low-salinity fluids. Thus, the pressure of the phase separation may be happened at 180–250 bar in stage II (Figure 13A), and the lithostatic depth waa about between 2.19 and 2.45 km. Furthermore, the entrapment pressure would increase because of the addition of CO_2 (Bowers and Helgeson, 1983; Peng et al., 2016; Wang Y. H et al., 2018). Fluid would increase the pressure by approximately 100 bar at 600°C when the addition of 5 mol% CO_2 to a 4 wt% NaCl equiv. It is consistent with the calculated pressure (<500 bar) of C-type inclusions (Figure 13B).

In the quartz–galena–sphalerite stage, the mineralizing fluids show features of moderate temperatures (163–347°C) and low salinities (0.87 wt%–8.94 wt% NaCl equiv.). In contrast to the quartz–molybdenite stage, temperature decreases limitedly, whereas salinity increases sharply. The fluids show an apparent trend towards the input of the meteoric water (as discussed above; Figure 9). As the magma cools and crystallizes, the upwelling fluid no longer intersects the two-phase surface due to the lack of power and heat from the magma (Shinohara and Hedenquist, 1997). However, when the temperature dropped below 400°C, which is considered to be the transition temperature from lithostatic to hydrostatic conditions caused by the change from ductile to brittle behavior of the system (Fournier, 1999), the pressure of the fluid would fall rapidly and result in the supercritical fluid intersecting the two-phase surface again and boil to form two fluids with different properties, medium-to-high-salinity and low-salinity fluids (Shu et al., 2013; Zhu et al., 2015). The influence of CO_2 to pressure estimate can be ignored as the C-type inclusions occupy a very small fraction. In conclusion, the pressure of the fluid in this stage is ~150 bar (Figure 13A), corresponding to a depth of ~0.56 km in the hydrostatic condition. At last, in the quartz–calcite stage (IV), the low temperatures (151–231°C) and low salinities (0.88 wt%–11.34 wt% NaCl equiv) may be caused by mixing with meteoric water.

6.4 Mechanisms of ore precipitation

6.4.1 Mechanisms of molybdenite precipitation

There are four mechanisms that can lead to metal complex destabilization and ore precipitation, which are fluid boiling, fluid mixing, reduction in temperature, pressure and salinity, and fluid–rock interactions (Li et al., 2012; Wang S et al., 2018). First, cooling causes a significant reduction in the solubility of molybdenum in porphyry (Ulrich and Mavrogenes, 2008),

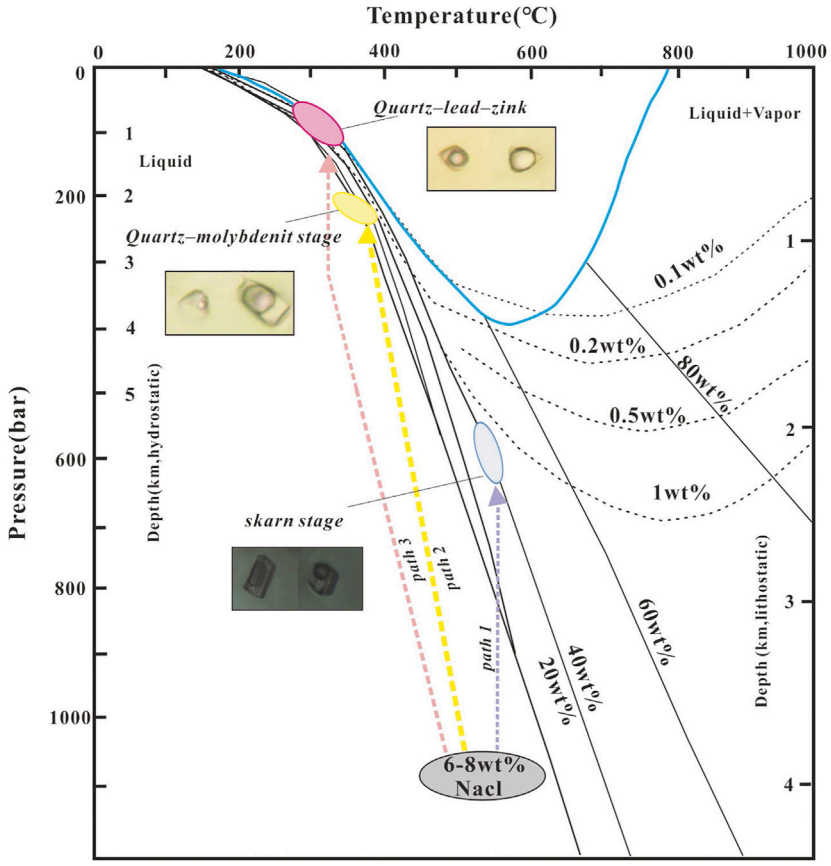

FIGURE 14
Fluid evolution paths of the Shibaogou Mo (Mo) deposit (after Meinert et al., 2003; Shu et al., 2013; Peng et al., 2016). The initial fluids exsolved from the deep magma chamber are assumed supercritical magmatic fluids with an initial salinity of 6–8 wt% NaCl equiv. (Hedenquist and Lowenstern, 1994). These fluids followed three different cooling paths: (1) path 1 shows the fluid trajectory forming skarn (513–550 °C, 580–650 bar, and 2.19–2.45 km under a lithostatic condition); (2) path 2 shows the trajectory forming Mo-dominated mineralization (324–387 °C, 180–250 bar, and 0.49–0.94 km under a hydrostatic depth); (3) path 3 shows the trajectory forming quartz–galena–sphalerite stage of mineralization (303–347 °C, <150bar, and <0.56 km under a hydrostatic depth). For details see text.

while in the Shibaogou Mo deposit, the temperature decreased less significantly from skarn stage to quartz–molybdenite stage with still high temperatures (>300°C) excluding the possibility of temperature-decreasing mechanism. Second, the intrusion of atmospheric fluids causes a reduction in both temperature and salinity, which reduces the solubility of molybdenum, this process is vital in during the precipitation of molybdenite (Shu and Lai, 2017). However, as showed in Figure 10, the ore-forming fluids in the quartz–molybdenite stage were dominated by magmatic fluids. Therefore, the mixing of ore-forming fluids with meteoric water may have little effect on the precipitation process of molybdenite in the Shibaogou deposit.

Third, as revealed by the close spatial relationship between the alteration mineral and mineralization, the ore-forming process was genetically related to the alteration process. In addition, the H–O isotopic data (Figure 10) indicate that fluid–rock interactions occurred in the quartz–molybdenite stage. Thus, we speculate that a more acidic fluid (e.g., pH = 3.9 in the Bismark skarn deposit; Bertelli et al., 2009) which was separated from the source magma (Sillitoe, 2010), reacts with pre-ore-stage skarn minerals (garnet, pyroxene, and wollastonite), which forcing the pH to rise and consequently leading to sulfide precipitation (Bertelli et al., 2009). This mechanism is also evidenced by the numerous C-type fluid inclusions, which is produced by the water-rock reaction of the intrusion of the shibaogou granite porphyry into the Guandaokou group in quartz formed in the stage II. Fourth, the intensity of the fluid boiling in obvious, which is evidenced by coexisting of less H-type, V-type and L-type inclusion.

As a result, the fluid boiling and fluid–rock interactions may be the important processes in controlling molybdenum mineralization in the Shibaogou molybdenum–lead–zinc deposit.

6.4.2 Mechanisms of galena and sphalerite precipitation

Chloride and hydrosulfide complexes are the main medium to transport sphalerite and galena in hydrothermal fluids (Tagirov and Seward, 2010; Zhong et al., 2015). Especially under high-temperature and moderate-salinity conditions, chloride complexes are more stable than sulfide species (Zhang et al., 2016). We infer that galena and sphalerite are transported through chloride complexes because the zinc-lead mineralization fluids of the Shibaogou deposit are characterized by medium to high temperatures, mainly 200–250°C. From the stage I to stage III, the intensity of the fluid boiling gradually descends. In stage III, the fluid boiling event has been not obvious which is evidenced by the declining number of coexisting V-type and L-type fluid inclusion assemblages. Therefore, fluid boiling is not the main reason for the precipitation of galena and sphalerite. The hydrothermal fluid temperatures and salinities of the Shibaogou deposit decreased strikingly from skarn Stage (500–550°C; 0.35 wt%–46.05 wt% NaCl equiv.) to quartz–galena–sphalerite stage (200–250°C; 0.87 wt%–8.94 wt% NaCl equiv.) (Figure 9). Galena and sphalerite are likely to have precipitated in the Shibaogou deposit as a result of the considerable reduction in temperature since chloride complexes of sphalerite and sphalerite are destabilized with a significant decrease in temperature (Reed and Palandri, 2006).

6.5 Tectonic implications

A large amount of geochronological data are analyzed and sorted out, and dividing the molybdenum mineralization in the East Qinling orogenic belt. The molybdenum mineralization in the East Qinling orogenic belt can be divided into three periods from the middle and late Triassic to the middle and late Cretaceous (Mao et al., 2008). Molybdenite Re-Os geochronology in the Shibaogou deposit yields ^{187}Re-^{187}Os isochron age of 146.3–151.2 Ma, indicating that it was the product of the subduction of the Paleo-Pacific plate under Eurasia (Mao et al., 2011). The Late Mesozoic tectonic regime led to the subduction event, which was characterized by a transition from post-collision compression to extension in eastern China, leading to an intense tectonic-magmatic events (Yang et al., 2018b; Li et al., 2018; Xue et al., 2018, 2019, 2020; Tang et al., 2019; Yang et al., 2019). During the period from the Late Jurassic to the Early Cretaceous, the lithosphere in eastern China experienced a strong thinning process (Yang et al., 2018a; Yang et al., 2018b; Yang et al., 2019), the asthenospheric upwelling and underplating triggered deep penetration of the lower crust and injection of mafic magma into the mantle (Mao et al., 2008). The felsic magma rises to the magma chamber of the upper crust with a small amount of mafic magma, and the interaction between felsic and mafic forms monzonitic granite and high-fractionated I-type granite porphyries formed by segregation crystallization rock (Mao et al., 2005, 2013; Li et al., 2018; Yang et al., 2019). More and more melts are rapidly released from the fractionated magma chambers, and the melts carrying rich mineral-forming materials gradually rise from the magma chambers to higher levels and into the crustal extent. The Shibaogou Mo–Pb–Zn deposit was created as a result of the release of ore-bearing fluids following the emplacement of the Shibaogou granitic intrusions.

7 Conclusion

1) Molybdenite Re-Os model ages of the Shibaogou deposit vary from 146.3 ± 2.6 to 151.2 ± 2.2 Ma, with a weighted mean age of 148.9 ± 1.7 Ma.
2) The H–O–S–Pb isotope indicates that the ore-forming fluid came from magmatic water in the early stage, and was gradually added by meteoric water in the later stage, and the ore-forming material mainly came from the Shibaogou granite porphyry intrusion.
3) The major factors controlling Mo precipitation are boiling and fluid–rock interaction during this stage. The decrease in temperature and salinity are the main factors controlling Pb–Zn precipitation at the Shibaogou deposit.
4) The complex evolution of the ore-forming fluids was related to the subduction of the Paleo-Pacific Plate, which induced the lithospheric thinning in the eastern China and the post-collisional extension triggered resulting from the Yangtze Craton and NCC collision.

Data availability statement

The original contributions presented in the study are included in the article/Supplementary Material; further inquiries can be directed to the corresponding author.

Author contributions

GW, MG, SY, and WY revised the manuscript, conceived the experiments, and contributed to the data interpretation. The fieldwork and preliminary study of samples were carried out by HY and PW. NG and YF conducted the geochemical analyses and reviewed both the science and English language. YX led data interpretations and manuscript preparation through discussion with all co-authors. All authors have read and agreed to the published version of the manuscript.

Funding

The research was supported by the China Ministry of Science and Technology, Ministry of Land and Resources Public Service

Sectors Fund (Grant No. 201111007-4) and Scientifific research Project of Geological and Mineral Exploration and Development Bureau of Henan Province (2021KC-8, 202202).

Acknowledgments

The authors would like to thank Liwei Xue, MG, YF, HY, Yi Cao, Yulin Chang, SY, and WY for their assistance with the experiments.

Conflict of interest

Author YF was employed by Luanchuan Xinshu Weibo Mining Co., Ltd.

The remaining authors declare that the research was conducted in the absence of any commercial or financial relationships that could be construed as a potential conflict of interest.

The reviewer AL declared a shared affiliation with the authors YX, GW, MG, WY, and SY to the handling editor at time of review.

Publisher's note

All claims expressed in this article are solely those of the authors and do not necessarily represent those of their affiliated organizations, or those of the publisher, the editors, and the reviewers. Any product that may be evaluated in this article, or claim that may be made by its manufacturer, is not guaranteed or endorsed by the publisher.

References

AudeÂtat, A., and Gunther, D. (1999). Mobility and H_2O loss from fluid inclusions in natural quartz crystals. *Contributions Mineralogy Petrology* 137, 1–14. doi:10.1007/s004100050578

Bakker, R. J., and Jansen, J. B. H. (1994). A mechanism for preferential H_2O leakage from fluid inclusions in quartz, based on TEM observations. *Contr. Mineral. Pet.* 116, 7–20. doi:10.1007/bf00310686

Bao, Z. W., Wang, C. Y., Zhao, T., Li, C., and Gao, X. (2014). Petrogenesis of the Mesozoic granites and Mo mineralization of the Luanchuan ore field in the East Qinling Mo mineralization belt, Central China. *Ore Geol. Rev.* 57, 132–153. doi:10.1016/j.oregeorev.2013.09.008

Bertelli, M., Baker, T., Cleverley, J. S., and Ulrich, T. (2009). Geochemical modelling of a Zn-Pb skarn: Constraints from LA-ICP-MS analysis of fluid inclusions. *J. Geochem. Explor.* 102, 13–26. doi:10.1016/j.gexplo.2008.11.015

Bowers, T. S., and Helgeson, H. C. (1983). Calculation of the thermodynamic and geochemical consequences of nonideal mixing in the system H_2O-CO_2-NaCl on phase relations in geologic systems: Equation of state for H_2O-CO_2-NaCl fluids at high pressures and temperatures. *Geochimica Cosmochimica Acta* 47, 1247–1275. doi:10.1016/0016-7037(83)90066-2

Bowers, T. S. (1991). The deposition of gold and other metals: Pressureinduced fluid immiscibility and associated stable isotope signatures. *Geochimica Cosmochimica Acta* 55, 2417–2434. doi:10.1016/0016-7037(91)90363-a

Cao, H. W., Zhang, S. T., Santosh, M., Zheng, L., Tang, L., Li, D., et al. (2015). The Luanchuan Mo-W-Pb-Zn-Ag magmatic-hydrothermal system in the East Qinling metallogenic belt, China: Constrains on metallogenesis from C-H-O-S-Pb isotope compositions and Rb-Sr isochron ages. *J. Asian Earth Sci.* 111, 751–780. doi:10.1016/j.jseaes.2015.06.005

Catchpole, H., Kouzmanov, K., Putlitz, B., Seo, J. H., and Fontbote, L. (2015). Zoned base metal mineralization in a porphyry system: Origin and evolution of mineralizing fluids in the Morococha district, Peru. *Econ. Geol.*, 110, 39–71, doi:10.2113/econgeo.110.1.39

Collins, P. L. F. (1979). Gas hydrates in CO_2-bearing fluid inclusions and the use of freezing data for estimation of salinity. *Econ. Geol.* 74, 1435–1444. doi:10.2113/gsecongeo.74.6.1435

Deng, X. H., Chen, Y. J., Santosh, M., and Yao, J. M. (2013). Genesis of the 1.76 Ga zhaiwa Mo–Cu and its link with the xiong'er volcanics in the North China craton: Implications for accretionary growth along the margin of the columbia supercontinent. *Precambrian Res.* 227, 337–348. doi:10.1016/j.precamres.2012.02.014

Driesner, T., and Heinrich, C. A. (2007). The system H_2O NaCl. Part I: Correlation formulae for phase relations in temperature pressure composition space from 0 to 1000 C, 0 to 5000 bar, and 0 to 1 X NaCl. *Geochimica Cosmochimica Acta* 71, 4880–4901. doi:10.1016/j.gca.2006.01.033

Du, A. D., Zhao, D. M., Wang, S. X., Sun, D. Z., and Liu, D. Y. (2001). Precise ReeOs dating for molybdenite by IDeNTIMS with carius tube sample preparation. *Rock Mineral Analysis* 20, 247 (in Chinese with English abstract). doi:10.15898/j.cnki.11-2131/td.2001.04.002

Duan, S., G., Xue, C. J., Chi, G. X., Liu, G. Y., Yan, C. H., Feng, Q. W., et al. (2011). Ore geology, fluid inclusion, and S- and Pb-isotopic constraints on the genesis of the chitudian Zn-Pb deposit, southern margin of the north China craton. *Resour. Geol.* 61, 224–240. doi:10.1111/j.1751-3928.2011.00160.x

Duan, S. G., Xue, C. J., Liu, G. Y., Yan, C. H., Feng, Q. W., Song, Y. W., et al. (2010). Geology and sulfur isotope geochemistry of lead-zinc depositsin Luanchuan district, Henan province, China. *Earth Sci. Front.* 17, 375(in Chinese with English abstract).

Fallick, A. E., Macaulay, C. I., and Haszeldine, R. S. (1993). Implications of linearly correlated oxygen and hydrogen isotopic compositions for kaolinite and illite in the magnus sandstone, north sea. *Clays Clay Min.* 41, 184–190. doi:10.1346/ccmn.1993.0410207

Fournier, R. O. (1999). Hydrothermal processes related to movement of fluid from plastic into brittle rock in the magmatic-epithermal environment. *Econ. Geol.* 94, 1193–1211. doi:10.2113/gsecongeo.94.8.1193

Gehrig, M., Lentz, H., and Franck, E. (1986). The system water-carbon dioxide-sodium chloride to 773 K and 300 MPa. *Berichte Bunsenges. fur Phys. Chem.* 90, 525–533. doi:10.1002/bbpc.19860900606

Gemmell, J. B., Zantop, H., and Meinert, L. D. (1992). Genesis of the Aguilar zinc-lead-silver deposit, Argentina; contact metasomatic vs. sedimentary exhalative. *Econ. Geol.* 87 (8), 2085–2112. doi:10.2113/gsecongeo.87.8.2085

Guo, B. (2018). *Geochemical and geological characteristics of the concealed granitic batholith and Yuku Mo-W deposit at the Luanchuan ore cluster*. BeijingBeijing): China University of Geosciences.

Hedenquist, J. W., and Lowenstern, J. B. (1994). The role of magmas in the formation of hydrothermal ore deposits. *Nature* 370, 519–527. doi:10.1038/370519a0

Hedenquist, J. W., and Richards, J. P. (1998). The influence of geochemical techniques on the development of genetic models for porphyry copper deposits. *Rev. Econ. Geol.* 10, 235

Hoefs, J. (2009). *Stable isotope geochemistry*. Berlin Heidelberg: Springer-Verlag.

Hua, R. M., and Mao, J. W. (1999). A preliminary discussion on the Mesozoic metallogenic explosion in East China. *Mineral. Deposits* 18, 300

Huang, D. H., Nie, F. J., Wang, Y. C., and Jiang, X. J. (1984). Lead isotopic compositions of molybdenum deposits in East Qinling as applied to the problem of ore sources. *Min. Deposita* 3, 20(in Chinese with English abstract).

Hugh, P., and Taylor, J. R. (1974). The application of oxygen and hydrogen isotope studies to problems of hydrothermal alteration and ore deposition. *Econ. Geol.* 60, 843–883. doi:10.2113/gsecongeo.69.6.843

Kodõera, P., Lexa, J., and Fallick, A. E. (2010). Formation of the Vysoká–Zlatno Cu–Au skarn–porphyry deposit, Slovakia. *Min. Depos.* 45, 817–843. doi:10.1007/s00126-010-0304-9

Lei, X. F., Duan, D. F., Jiang, S. Y., and Xiong, S. F. (2018). Ore-forming fluids and isotopic (H-O-C-S-Pb) characteristics of the fujiashan-longjiaoshan skarn W-Cu-

(Mo) deposit in the edong district of hubei province, China. *Ore Geol. Rev.* 102, 386–405. doi:10.1016/j.oregeorev.2018.09.019

Li, D., Han, J., Zhang, S., Yan, C., Cao, H., and Song, Y. (2015). Temporal evolution of granitic magmas in the Luanchuan metallogenic belt, east Qinling Orogen, central China: Implications for Mo metallogenesis. *J. Asian Earth Sci.* 111, 663–680. doi:10.1016/j.jseaes.2015.05.017

Li, H. M., Ye, H. S., Mao, J. W., Wang, D. H., Chen, Y. C., Qu, W. J., et al. (2007). Re-Os dating of molybdenites from Au (-Mo) deposits in Xiaoqinling gold are district and its geological significance. *Mineral. Deposits* 26, 417(in Chinese with English abstract).

Li, H. M., Ye, H. S., Wang, D. H., Chen, Y. C., Qu, W. J., and Du, A. D. (2009). Re-Os dating of molybdenites from Zhaiwa Mo deposit in Xiong'er Mountain, Western Henan Province, and its geological significance. *Mineral. Deposits* 28, 133(in Chinese with English abstract).

Li, N., Chen, Y.-J., Santosh, M., and Pirajno, F. (2018). Late mesozoic granitoids in the qinling orogen, central China, and tectonic significance. *Earth. Sci. Rev.* 182, 141–173. doi:10.1016/j.earscirev.2018.05.004

Li, N., Chen, Y.-J., Ulrich, T., and Lai, Y. (2011). Fluid inclusion study of the Wunugetu Cu-Mo deposit, Inner Mongolia, China. *Min. Depos.* 47, 467–482. doi:10.1007/s00126-011-0384-1

Li, N., Chen, Y. J., Pirajno, F., and Ni, Z. y. (2013). Timing of the Yuchiling giant porphyry Mo system, and implications for ore Genesis. *Min. Depos.* 48, 505–524. doi:10.1007/s00126-012-0441-4

Li, N., Ulrich, T., Chen, Y. J., Thomsen, T. B., Pease, V., and Pirajno, F. (2012). Fluid evolution of the yuchiling porphyry Mo deposit, East Qinling. China. *Ore Geol. Rev.* 48, 442–459. doi:10.1016/j.oregeorev.2012.06.002

Li, N., Yang, F. Q., and Zhang, Z. X. (2020). Fluid inclusions and isotope (C, H, O, S, He, and Ar) study of the Xiaobaishitou skarn W-(Mo) deposit, East Tianshan, NW China. *Ore Geol. Rev.* 122, 103520. doi:10.1016/j.oregeorev.2020.103520

Liu, G. Y., Yan, C. H., Song, Y. W., and Duan, S. G. (2007). Characteristics and Genesis of Chitudian lead-zinc deposits in Luanchuan county. *Geol. Surv. Res.* 30, 263

Lu, H. Z., Fan, H. R., Ni, P., Ou, G. X., Shen, K., Zhang, W. H., et al. (2004). *Fluid inclusion* (Beijing: Science Press), 1–487. (in Chinese with English abstract).

Ludwig, K. R. (2003). User's manual for isoplot 3.0" in *A Geochronological Toolkit Microsoft Excel*, 4. Berkeley Geochron Center Special publication, 1

Luo, M. J., Zhang, F. M., Dong, Q. Y., Xu, Y. R., Li, S. M., and Li, K. H. (1991). *Molybdenum deposits in China, zhengzhou*. Henan Science Technology Press.

Lynch, J. V. G., Longstaffe, F. J., and Nesbitt, B. E. (1990). Stable isotopic and fluid inclusion indications of large-scale hydrothermal paleoflow, boiling, and fluid mixing in the Keno Hill Ag-Pb-Zn district, Yukon Territory, Canada. *Geochimica Cosmochimica Acta* 54, 1045–1059. doi:10.1016/0016-7037(90)90438-q

Macaulay, C. I., Fallick, A. E., Haszeldine, R. S., and Graham, C. M. (2000). Methods of laser-based stable isotope measurement applied to diagenetic cements and hydrocarbon reservoir quality *Clay Min.*, 35, 313–322, doi:10.1180/000985500546684

Mao, J., Wang, Y., Li, H., Pirajno, F., Zhang, C., and Wang, R. (2008). The relationship of mantle-derived fluids to gold metallogenesis in the Jiaodong Peninsula: Evidence from D-O-C-S isotope systematics. *Ore Geol. Rev.*, 33, 361–381, doi:10.1016/j.oregeorev.2007.01.003

Mao, J. W., Pirajno, F., Xiang, J. F., Gao, J. J., Ye, H. S., Li, Y. F., et al. (2011). Mesozoic molybdenum deposits in the east Qinling-Dabie orogenic belt: Characteristics and tectonic settings. *Ore Geol. Rev.* 43, 264–293. doi:10.1016/j.oregeorev.2011.07.009

Mao, J. W., Xie, G. Q., Zhang, Z. H., Li, X. F., Wang, Y. T., Zhang, C. Q., et al. (2005). Mesozoic large-scale metallogenic pulses in North China and corresponding geodynamic setting. *Acta Petrol. Sin.* 21, 169(in Chinese with English abstract).

Mao, W., Li, X., and Yang, F. (2013). Zircon LA-ICP-MS U-Pb ages of granites at Dabaoshan polymetallic deposit and its geological significance, Guangdong, South China. *Acta Petrol. Sin.* 29, 4104(in Chinese with English abstract).

Marcoux, É., Breillat, N., Guerrot, C., Négrel, P., Hmima, S. B., and Selby, D. (2019). Multi-isotopic tracing (Mo, S, Pb, Re, Os) and Genesis of the Mo W Azegour skarn deposit (High-Atlas, Morocco). *J. Afr. Earth Sci.*, 155, 109–117, doi:10.1016/j.jafrearsci.2019.04.007

Meinert, L. D., Dipple, G. M., and Nicolescu, S. (2005). World skarn deposits. *Econ. Geol. 100th Anniv.* Volume, 299

Meinert, L. D., Hedenquist, J. W., Satoh, H., and Matsuhisa, Y. (2003). Formation of anhydrous and hydrous skarn in Cu-Au ore deposits by magmatic fluids. *Econ. Geol.* 98, 147–156. doi:10.2113/gsecongeo.98.1.147

Newberry, R. J., and Swanson, S. E. (1986). Scheelite skarn granitoids: An evaluation of the roles of magmatic source and process. *Ore Geol. Rev.* 1 (1), 57–81. doi:10.1016/0169-1368(86)90005-3

Ouyang, H. G., Mao, J. W., Santosh, M., Zhou, J., Zhou, Z. H., Wu, Y., et al. (2013). Geodynamic setting of Mesozoic magmatism in NE China and surrounding regions: Perspectives from spatio-temporal distribution patterns of ore deposits. *J. Asian Earth Sci.* 78, 222–236. doi:10.1016/j.jseaes.2013.07.011

Peng, H. J., Mao, J. W., Hou, L., Shu, Q. H., Zhang, C. Q., Liu, H., et al. (2016). Stable isotope and fluid inclusion constraints on the source and evolution of ore fluids in the Hongniu-Hongshan Cu skarn deposit, Yunnan Province. China. *Econ. Geol.* 111, 1369–1396. doi:10.2113/econgeo.111.6.1369

Qi, J. P. (2006). *Geology, geochemistry and genesis of vein type lead-zinc-silver deposits in Luanchuan*. HenanBeijing: Peking University, 1–114. (in Chinese with English abstract).

Reed, M., and Palandri, J. (2006). *A database of equilibrium constants for minerals and aqueous species*. Eugene, OregonH06: University of OregonSOLTHERM.

Richards, J. P. (2011). Magmatic to hydrothermal metal fluxes in convergent andcollided margins. *Ore Geol. Rev.* 40, 1–26. doi:10.1016/j.oregeorev.2011.05.006

Richards, J. P. (2009). Postsubduction porphyry Cu-Au and epithermal Au deposits: Products of remelting of subduction-modified lithosphere. *Geology* 37, 247–250. doi:10.1130/g25451a.1

Roedder, E., and Bodnar, R. J. (1980). Geologic pressure determinations fromfluid inclusion studies. *Annu. Rev. Earth Planet. Sci.* 8, 263–301. doi:10.1146/annurev.ea.08.050180.001403

Roedder, E. (1984). *Fluid inclusions, review in mineralogy*, 12. Mineralogical Society of America, 644

Shinohara, H., and Hedenquist, J. W. (1997). Constraints on magma degassing beneath the Far Southeast porphyry Cu-Au deposit, Philippines. *J. Petrology* 38, 1741–1752. doi:10.1093/petroj/38.12.1741

Shu, Q. H., and Lai, Y. (2017). *Fluid inclusion and oxygen isotope constraints on the origin and hydrothermal evolution of the Haisugou Porphyry Mo deposit in the Northern Xilamulun District, NE China*. Geofluids. 1

Shu, Q. H., Lai, Y., Sun, Y., Wang, C., and Meng, S. (2013). Ore Genesis and hydrothermal evolution of the Baiyinnuoer zinc-lead Skarn deposit, Northeast China evidence from isotopes (S, Pb) and fluid inclusions. *Econ. Geol.* 108, 835–860. doi:10.2113/econgeo.108.4.835

Sillitoe, R. H. (2010). Porphyry copper systems. *Econ. Geol.* 105, 3–41. doi:10.2113/gsecongeo.105.1.3

Smoliar, M. I., Walker, R. J., and Morgan, J. W. (1996). Re-Os ages of group IIA, IIIA, IVA and IVB iron meteorites. *Science* 271, 1099–1102. doi:10.1126/science.271.5252.1099

Soloviev, S. G., Kryazhev, S. G., and Dvurechenskaya, S. S. (2019). Geology, mineralization, and fluid inclusion characteristics of the Meliksu reduced tungsten skarn deposit, Alai Tien Shan, Kyrgyzstan: Insights into conditions of formation and regional links to gold mineralization. *Ore Geol. Rev.* 111, 103003. doi:10.1016/j.oregeorev.2019.103003

Soloviev, S. G., and Kryazhev, S. G. (2018a). Magmatic-hydrothermal evolution at the Lyangar redox-intermediate tungsten-molybdenum skarn deposit, Western Uzbekistan, Tien Shan: Insights from igneous petrology, hydrothermal alteration, and fluid inclusion study. *Lithos* 316-317, 154–177. doi:10.1016/j.lithos.2018.07.015

Soloviev, S. G., and Kryazhev, S. G. (2018b). Tungsten mineralization in the Tien Shan Gold Belt: Geology, petrology, fluid inclusion, and stable isotope study of the Ingichke reduced tungsten skarn deposit, Western Uzbekistan. *Ore Geol. Rev.* 101, 700–724. doi:10.1016/j.oregeorev.2018.08.020

Stein, H. J., Markey, R. J., Morgan, J. W., Hannah, J. L., and Scherstén, A. (2001). The remarkable Re-Os chronometer in molybdenite: How and why it works. *Terra nova*. 13, 479–486. doi:10.1046/j.1365-3121.2001.00395.x

Stein, H., Scherstén, A., Hannah, J., and Markey, R. (2003). Subgrain-scale decoupling of Re and ^{187}Os and assessment of laser ablation ICP-MS spot dating in molybdenite. *Geochimica Cosmochimica Acta* 67, 3673–3686. doi:10.1016/s0016-7037(03)00269-2

Sterner, S. M., Hall, D. L., and Bodnar, R. J. (1988). Synthetics fluid inclusions: V. Solubility relations in the system NaCl-KCl-H_2O under vapor-saturated conditions. *Geochimica Cosmochimica Acta* 52, 989–1005. doi:10.1016/0016-7037(88)90254-2

Suzuki, K., Shimizu, H., and Masuda, A. (1996). ReOs dating of molybdenites from ore deposits in Japan: Implication for the closure temperature of the ReOs system for molybdenite and the cooling history of molybdenum ore deposits. *Geochimica Cosmochimica Acta* 60, 3151–3159. doi:10.1016/0016-7037(96)00164-0

Tagirov, B. R., and Seward, T. M. (2010). Hydrosulfide sulfide complexes of zinc to 250 °C and the thermodynamic properties of sphalerite. *Chem. Geol.* 269, 301–311. doi:10.1016/j.chemgeo.2009.10.005

Tang, L., Hu, X. K., Santosh, M., Zhang, S. T., Spencer, C. J., Jeon, H., et al. (2019). Multistage processes linked to tectonic transition in the Genesis of orogenic gold deposit: A case study from the shanggong lode deposit, East Qinling, China. *Ore Geol. Rev.* 111, 102998. doi:10.1016/j.oregeorev.2019.102998

Tang, L., Wagner, T., Fusswinkel, T., Zhang, S., Hu, X., and Schlegel, T. (2022). Fluid inclusion evidence for the magmatic-hydrothermal evolution of closely linked porphyry Au, porphyry Mo, and barren systems, East Qinling, China. *GSA Bull.* 134, 1529–1548. doi:10.1130/b36170.1

Tang, L., Zhao, Y., Zhang, S., Sun, L., Hu, X., Sheng, Y., et al. (2021). Origin and evolution of a porphyry-breccia system: Evidence from zircon U-Pb, molybdenite Re-Os geochronology, *in situ* sulfur isotope and trace elements of the qiyugou deposit, China. *Gondwana Res.* 89, 88–104. doi:10.1016/j.gr.2020.08.013

Ulrich, T., and Mavrogenes, J. (2008). An experimental study of the solubility of molybdenum in H_2O and KCl-H_2O solutions from 500°C to 800°C, and 150 to 300MPa. *Geochimica Cosmochimica Acta* 72, 2316–2330. doi:10.1016/j.gca.2008.02.014

Veksler, I. V. (2004). Liquid immiscibility and its role at the magmatic-hydrothermal transition: A summary of experimental studies. *Chem. Geol.* 210, 7–31. doi:10.1016/j.chemgeo.2004.06.002

Wang, G. W., Li, R. X., Carranza, E. J. M., Zhang, S. T., Yan, C. H., Zhu, Y. Y., et al. (2015). 3D geological modeling for prediction of subsurface Mo targets in the Luanchuan district, China. *Ore Geol. Rev.* 71, 592–610. doi:10.1016/j.oregeorev.2015.03.002

Wang, S., Li, B., Zhang, X., Wang, P., Chao, W., Ye, H., et al. (2019). Genesis of the Huoshenmiao Mo deposit in the Luanchuan ore district, China: Constraints from geochronology, fluid inclusion, and H-O-S isotopes. *Geosci. Front.* 10, 331–349. doi:10.1016/j.gsf.2017.12.020

Wang, S, S., Zhang, Y., Zhang, H., Zhu, A. M., Wang, H. M., Shi, X. F., et al. (2018). Petrogenesis and tectonic setting of the mesozoic Huoshenmiao intrusion in the luanchuan ore district, henan province, north China. *J. Asian Earth Sci.* 160, 239–257. doi:10.1016/j.jseaes.2018.02.019

Wang, Y. H, Y. H., Zhang, F. F., Liu, J. J., Xue, C. J., Li, B. C., and Xian, X. C. (2018). Ore Genesis and hydrothermal evolution of the Donggebi porphyry Mo deposit, Xinjiang, Northwest China: Evidence from isotopes (C, H, O, S, Pb), fluid inclusions, and molybdenite Re-Os dating. *Econ. Geol.* 113, 463–488. doi:10.5382/econgeo.2018.4558

Wei, Q. G., Yao, J. M., Zhao, T. P., Sun, Y. L., Yuan, Z. L., and Qiao, B. (2009). Discovery of a 1.9 Ga Mo deposit in the eastern qinling orogen: Molybdenite Re-Os ages of the longmendian Mo deposit in henan province. *Acta Petrol. Sin.* 25, 2747–2751. (in Chinese with English abstract).

Xu, B., Hou, Z., Griffin, W. L., Zheng, Y., Wang, T., Guo, Z., et al. (2021). Cenozoic lithospheric architecture and metallogenesis in southeastern Tibet. *Earth. Sci. Rev.* 214, 103472. doi:10.1016/j.earscirev.2020.103472

Xue, F., Santosh, M., Tsunogae, T., and Yang, F. (2019). Geochemical and isotopic imprints of early cretaceous mafic and felsic dyke suites track lithosphere-asthenosphere interaction and craton destruction in the North China Craton. *Lithos*, 326-327, 174–199, doi:10.1016/j.lithos.2018.12.013

Xue, F., Santosh, M., Tsunogae, T., Yang, F., and Zhou, H. (2020). The Genesis of high Ba-Sr adakitic rocks: Insights from an Early Cretaceous volcanic suite in the central North China Craton. *Geol. J.* 55, 5398–5416. doi:10.1002/gj.3720

Xue, F., Wang, G. W., Santosh, M., Yang, F., Shen, Z. W., Kong, L., et al. (2018). Geochemistry and geochronology of ore-bearing and barren intrusions in the Luanchuan ore fields of East Qinling metallogenic belt, China: Diverse tectonic evolution and implications for mineral exploration. *J. Asian Earth Sci.* 157, 57–77. doi:10.1016/j.jseaes.2017.04.027

Xue, F, F., Santosh, M., Kim, S. W., Tsunogae, T., and Yang, F. (2021). Thermo-mechanical destruction of archean cratonic roots: Insights from the mesozoic laiyuan granitoid complex, north China craton. *Lithos* 400-401, 106394–106401. doi:10.1016/j.lithos.2021.106394

Xue, L. W, L. W., Wang, G. W., Tang, L., Cao, Y., Du, J. G., Du, Y. S., et al. (2021). Genesis and hydrothermal evolution of the Zhazigou skarn W (Mo) deposit, East Qinling, China: Constraints from fluid inclusions and H-O-S-Pb isotopes. *Ore Geol. Rev.* 138, 104374. doi:10.1016/j.oregeorev.2021.104374

Yan, C. H., Liu, G. Y., Peng, Y., Song, Y. W., Wang, J. Z., Zhao, R. J., et al. (2009). *The metallogenetical characteristics of the lead–zinc–silver deposits in southwest Henan*. Beijing: Geological Press, 1–365. (in Chinese).

Yan, C. H. (2004). *Study on inner structure of lead–zinc–silver mineralization system in Eastern Qinling*. Beijing: Geological Press, 1–144. (in Chinese with English abstract).

Yang, F., Santosh, M., and Kim, S. W. (2018b). Mesozoic magmatism in the eastern North China Craton: Insights on tectonic cycles associated with progressive craton destruction. *Gondwana Res.* 60, 153–178. doi:10.1016/j.gr.2018.04.003

Yang, F., Santosh, M., and Tang, L. (2018a). Extensive crustal melting during craton destruction: Evidence from the Mesozoic magmatic suite of Junan, eastern North China Craton. *J. Asian Earth Sci.* 157, 119–140. doi:10.1016/j.jseaes.2017.07.010

Yang, F., Xue, F., Santosh, M., Wang, G., Kim, S. W., Shen, Z., et al. (2019). Late mesozoic magmatism in the east qinling orogen, China and its tectonic implications. *Geosci. Front.* 10, 1803–1821. doi:10.1016/j.gsf.2019.03.003

Yang, Y., Liu, Z. J., and Deng, X. H. (2017). Mineralization mechanisms in the Shangfanggou giant porphyry-skarn Mo–Fe deposit of the east Qinling, China: Constraints from HO–C–S–Pb isotopes. *Ore Geol. Rev.* 81, 535–547. doi:10.1016/j.oregeorev.2016.06.026

Yang, Y. L., Ni, P., Pan, J. Y., Zhe, C., Ding, J. Y., and Wang, Q. (2020). Episodic fluid evolution in the formation of the largescale Luoyang Fe deposit, Fujian, eastern China. *Ore Geol. Rev.*, 120, 103412, doi:10.1016/j.oregeorev.2020.103412

Yang, Z. M., Hou, Z. Q., Chang, Z. S., Li, Q. Y., Liu, Y. F., Qu, H. C., et al. (2016). Cospatial Eocene and Miocene granitoids from the Jiru Cu deposit in Tibet: Petrogenesis and implications for the formation of collisional and postcollisional porphyry Cu systems in continental collision zones. *Lithos* 245, 243–257. doi:10.1016/j.lithos.2015.04.002

Yokoro, Y., Hanamuro, T., and Nakashima, K. (2013). Unique origin of skarn at the ohori base metal deposit, yamagata prefecture, NE Japan: C, O and S isotopic study. *Resour. Geol.*, 63, 384–393, doi:10.1111/rge.12017

Zajacz, Z., Halter, W. E., Pettke, T., and Guillong, M. (2008). Determination of fluid melt partition coefficients by LA-ICPMS analysis of co-existing fluid and silicate melt inclusions: Controls on element partitioning. *Geochimica Cosmochimica Acta* 72, 2169–2197. doi:10.1016/j.gca.2008.01.034

Zeng, Q., Sun, Y., Duan, X., and Liu, J. (2013). U-Pb and Re-Os geochronology of the Haolibao porphyry Mo-Cu deposit, NE China: Implications for a Late Permian tectonic setting. *Geological Magazine* 150 (6), 975–985. doi:10.1017/S0016756813000186

Zhang, F. F., Wang, Y. H., and Liu, J. J. (2016). Fluid inclusions and H–O–S–Pb isotope systematics of the Baishan porphyry Mo deposit in Eastern Tianshan, China. *Ore Geol. Rev.* 78, 409–423. doi:10.1016/j.oregeorev.2016.04.015

Zhang, Y. H. (2014). *Late-mesozoic tectonic-magama evolution and its relationship with mineralization in luanchuan county*. Master's thesis. Beijing: China University of Geosciences.

Zheng, Y. F. (1990). Sulfur isotope fractionation in magmatic systems: Models of Rayleigh distillation and selective flux. *Chin. J. Geochem.* 9, 27–45. doi:10.1007/bf02837946

Zhong, R. C., Brugger, J., Chen, Y. J., and Li, W. B. (2015). Contrasting regimes of Cu, Zn and Pb transport in ore-forming hydrothermal fluids. *Chem. Geol.* 395, 154–164. doi:10.1016/j.chemgeo.2014.12.008

Zhu, J. J., Hu, R., Richards, J. P., Bi, X., and Zhong, H. (2015). Genesis and magmatic-hydrothermal evolution of the yangla skarn Cu deposit, southwest China. *Econ. Geol.* 110, 631–652. doi:10.2113/econgeo.110.3.631